A phosphoinositide-based model of actin waves in frustrated phagocytosis

Marco A. Avila Ponce de León [a], Bryan Félix [a], Hans G. Othmer [a,*]

[a] School of Mathematics, University of Minnesota, Minneapolis, MN, USA

ABSTRACT

Phagocytosis is a complex process by which phagocytes such as lymphocytes or macrophages engulf and destroy foreign bodies called pathogens in a tissue. The process is triggered by the detection of antibodies that trigger signaling mechanisms that control the changes of the cellular cytoskeleton needed for engulfment of the pathogen. A mathematical model of the entire process would be extremely complicated, because the signaling and cytoskeletal changes produce large mechanical deformations of the cell. Recent experiments have used a confinement technique that leads to a process called frustrated phagocytosis, in which the membrane does not deform, but rather, signaling triggers actin waves that propagate along the boundary of the cell. This eliminates the large-scale deformations and facilitates modeling of the wave dynamics. Herein we develop a model of the actin dynamics observed in frustrated phagocytosis and show that it can replicate the experimental observations. We identify the key components that control the actin waves and make a number of experimentally-testable predictions. In particular, we predict that diffusion coefficients of membrane-bound species must be larger behind the wavefront to replicate the internal structure of the waves. Our model is a first step toward a more complete model of phagocytosis, and provides insights into circular dorsal ruffles as well.

© 2021 Elsevier Ltd. All rights reserved.

1. Introduction

The role of an immune system is to protect an organism from the disease-inducing effects of foreign agents such as bacterial cells, virus particles and other pathogens. It identifies its targets by recognizing specific molecules called antigens that are presented by pathogens. Recognition is mediated by antibodies secreted by plasma cells that bind to specific antigens, and phagocytes such as macrophages monitor their environment to detect, via receptors on their surface, cells coated with antibody molecules. When a sufficient density of receptors is occupied a process called phagocytosis is initiated, the result of which is that macrophages engulf and destroy the foreign agent.

Phagocytosis is a complex process that requires finely-coordinated deformation and restructuring of the membrane and the underlying cytoskeleton of the macrophage. The process of engulfment and destruction of the pathogen involves the internalization of it into large vacuoles called phagosomes, which subsequently undergo a process of maturation that ultimately leads to disposal of the vacuolar contents (see Fig. 1). This process is initi-

ated upon activation of the signaling machinery of many immune receptors, of which only a select few have been studied. One of the best understood signaling pathways that leads to particle engulfment in humans is activated by the Fc-gamma family of receptors (FcγR), following recognition of the antibody immunoglobulin (IgG).[1]

The signaling network controlled by the FcγRs has been studied extensively (Flannagan et al., 2012; Freeman and Grinstein, 2014; Roni, 2015; Levin et al., 2016; Rosales and Uribe-Querol, 2017), and all studies agree that receptor activation following engagement of the tagged particle leads to a sequence of spatial and temporal changes in phosphoinositides, Rho-family GTPases and actin nucleation-promoting factors. The spatio-temporal dynamics of these molecules control processes such as remodeling of the cytoskeleton, membrane fusion and the production of reactive oxygen intermediates, that are necessary for particle internalization. However, it is not clear how the molecular scale activation of FcγRs

---

* Corresponding author.
   E-mail address: othmer@umn.edu (H.G. Othmer).

[1] There are several different types of Fc (Fragment,crystallizable) receptors (abbreviated FcR), which are classified based on the type of antibody that they recognize. The Latin letter used to identify a type of antibody is converted into the corresponding Greek letter, which is placed after the 'Fc' part of the name. For example, those that bind the most common class of antibody, IgG, are called Fc-gamma receptors (FcγR). We will use this terminology throughout the paper.
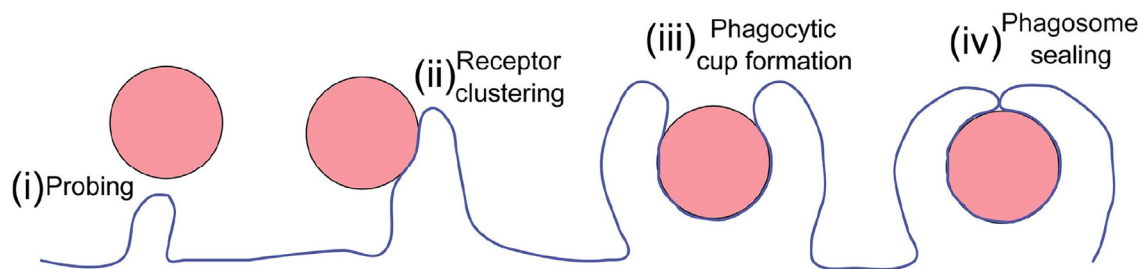
Fig. 1. Stages of phagocytosis. Reproduced from Levin et al. (2016) with permission.

leads to the observed micron-scale patterns of activation and inactivation of network components reflected in the propagating actin waves.

Recent reviews provide a broad overview of actin waves and survey evidence which suggests that they are associated with important cellular functions such as intracellular protein transport, cell protrusion, polarization and migration (Inagaki and Katsuno, 2017; Cheng et al., 2020). Known results suggest that actin waves can arise following stimulation of signaling pathways that control various cell functions, and due to the wide range of signaling pathways linked to actin waves, one would expect that the spatiotemporal organization of the various molecules driving these waves to differ as well. Thus while models based on an excitable activator-inhibitor mechanism driven by positive and negative feedback interactions can provide insight into the general structure required for wave generation (Allard and Mogilner, 2013), a more complete understanding of the mechanisms of wave generation and propagation requires the inclusion of the dynamics of the underlying signaling pathway (Khamviwath et al., 2013).

With the latter approach in mind, we propose a mathematical model of the FcγR signaling network which aims to capture the dynamics of the actin waves observed in Masters et al., 2016. The model is based on an extensive literature review of the essential proteins involved in FcγR-mediated phagocytosis, and integrates the interactions of Rho GTPases, phosphoinositides, nucleation-promoting factors, and actin monomers and filaments. To validate our results we used experimental results reported in Masters et al. (2016), in which mammalian macrophages undergo a process called 'frustrated phagocytosis'. In this process, cells displaying FcγRs are attracted to an IgG-coated plate, which activates the FcγRs. This leads to propagating circular wave fronts of concentrated filamentous actin on the surface-attached portion of the membrane that appear to be two-dimensional analogues of phagocytic cups observed in true phagocytosis. While a number of models of the process in other systems have been formulated (Arai et al., 2010; Bernitt et al., 2017; Hu et al., 2019; Khamviwath et al., 2013; Miao, 2019; Ryan et al., 2012; Vicker, 2002; Wasnik and Mukhopadhyay, 2014; Buracco et al., 2019; Liu et al., 2019) and are reviewed in Khatibi et al., 2018; Cheng et al., 2020; Beta et al., 2020, to our knowledge ours is the first detailed mechanistic model that can replicate the internal structure of the waves in this important biological process[2].

To begin, we discuss the conceptual mechanisms that have been proposed to explain the spatial amplification of the FcγR signal. We then present a review of the underlying biochemistry of FcγR-mediated phagocytosis and a description of the actin waves. This is followed by the development of the model and a description of the computational results that emerge. Finally, we compare the

model with those for actin waves in other systems, and discuss the implication of our results for dorsal ruffles.

2. The biochemistry of phagocytosis and the actin waves

The general consensus of the reviews mentioned earlier is that FcγR activation leads to a temporal sequence of activation and inactivation of many components that perform distinct, but complementary, roles in phagocytosis. Those thought to be essential are the Rho GTPases Cdc42 and Rac1[3] and the phosphoinositides PI(4,5)P2, PI(3,4)P2 and PI(3,4,5)P3 (PIP3 hereafter), the kinases and phosphatases PI5K, PI3K, PLCγ, SHIP2 and PTEN, and the nucleation-promoting factor N-WASP, branched actin, linear actin, and finally the second messenger lipid, DAG (see Fig. 2 for the components included in the model later). The observed timing, localization and function of these essential components is as follows.

PI(4,5)P2 is present in higher amounts relative to other phosphoinositides in the inner leaflet of the plasma membrane of resting phagocytes (Olivença et al., 2018). At the onset of phagocytosis in response to receptor activation, there is a transient biphasic response of both PI(4,5)P2 and F-actin, primarily branched F-actin, in the membrane region forming the phagocytic cup. Both increase rapidly followed by an abrupt decrease (Botelho, 2000; Scott et al., 2005) – with concentrated F-actin lagging slightly behind PI(4,5)P2. The drastic changes in local PI(4,5)P2 concentration can be explained via a feedback loop between PI(4,5) P2 and the type I family of 5-kinases that produce it from PI(4)P (Fairn et al., 2009).[4] Before and during the initial phase of phagocytosis these three kinases are predominantly localized at the plasma membrane, probably attracted by the charge negativity due primarily to PI(4,5)P2 (Fairn et al., 2009). Once on the membrane they are activated by the Rho-GTPases Rac1 and Cdc42 (Weernik et al., 2004). PIP3-mediated recruitment and subsequent tyrosine phosphorylation of PLCγ by the FcγR leads to hydrolysis of PI(4,5)P2 into DAG and IP3 (Falasca et al., 1998), which in turn reduces the surface charge of the membrane. PIP5Ks dissociate from the membrane in response to the drop in surface charge, thereby reducing PI(4,5)P2 synthesis and contributing to the rapid depletion of PI(4,5)P2 (Fairn et al., 2009). Other phosphatases such as OCRL and INPP5B contribute to the decrease by converting PI(4,5) P2 into PI(4)P (Bohdanowicz et al., 2012).

In phagocytes, as in many other cellular systems, PI(4,5)P2 is a major regulator of the actin cytoskeleton. Typically PI(4,5)P2

---

[2] Hereafter we will refer to these wave fronts of concentrated actin as the actin waves.

[3] The Rho GTPase family, some of whose best-studied members are Rho, Rac1 and Cdc42, are key factors in many cellular processes, including phagocytosis. Each Rho GTPase cycles between the active GTP-bound form on the plasma membrane and the inactive GDP-bound form in the cytosol, with conversions facilitated by GAPs, GEFs, and GDIs (Cherfils and Zeghouf, 2013; Guan et al., 2020; Salloum et al., 2020). Models of Rho GTPases have been made for numerous systems and a detailed review appears in Khatibi et al. (2018).

[4] The type I family of 5-kinases is comprised of three isoforms. However, in our model we assume the existence of a generic member of the family.

Fig. 2. The signal transduction steps following FcγR activation. Only membrane-localized components are shown, and all are placed in their approximate order of activation. Upon activation of FcγR (orange), downstream molecules enclosed in red boxes are activated/produced early while molecules in blue are activated/produced later. Lines with arrowheads represent activation, while lines with boxheads represent inhibition. Red lines represent fast interactions, blue lines represent slow interactions, and black lines represent feedback interactions. Together these interactions drive the time dynamics of actin (green). The steps shown represent high-level interactions – not molecular-level events. Despite not playing any role in the formation of the actin waves, we include DAG as a known late stage driver of phagocytosis (Botelho, 2000).

inhibits actin-binding proteins that promote filament disassembly or sequester monomers to inhibit growth, and activates proteins that induce branched actin filament assembly (Saarikangas et al., 2010), and this explains why concentrated actin follows the dynamics of PI(4,5)P2. Specifically, the nucleation-promoting factor N-WASP is recruited to the membrane by PI(4,5)P2 (Papayannopoulos, 2005), whereupon it is released from its auto-inhibited form by Cdc42, which enables recruitment and activation of the actin regulator Arp2/3 (Tomasevic, 2007). This in turn leads to the increase in the branched actin component of the cortex (Mullins et al., 2018). PI(4,5)P2 also inhibits the function of proteins such as cofilin, gelsolin, profilin and capping proteins that are involved in actin disassembly or monomer sequestration, and is also a known effector of ERM proteins, which link the cytoskeleton to the membrane (Saarikangas et al., 2010; Janmey, 2018). The temporal sequence of the foregoing events following FcγR activation serves as the starting point for development of the model described later.

The spatio-temporal pattern of PI(4,5)P2 and actin dynamics described above has been quantified in Masters et al. (2016), where total internal relfection fluorescence (TIRF) microscopy was used to image the ventral plasma membrane of macrophages undergoing frustrated phagocytosis. To produce frustrated phagocytosis, immune cells in suspension are exposed to a coverslip coated with IgG. Cells readily recognize and spread over the coverslip, activating exocytosis, cytoskeleton remodeling and cytokine production. The 2D nature of the phagocytic contact in this system renders it amenable to high-resolution imaging with TIRF and provides a fixed frame of reference. When macrophages were allowed to spread for five minutes, it was observed that around 10% of them displayed the actin waves described earlier. Application of a hypotonic shock, which can affect both membrane tension and cyto-

plasmic protein concentration, increased the number of cells displaying waves fourfold. In both cases, the waves were restricted to the substrate-attached surface.

The response of the actin cortex in attached cells to hypotonic shock is dramatic. An initially-small decrease in actin cortex density expands to cover a $10\mu m$ diameter region of the ventral plasma membrane within 100 s. Throughout the region PI(4,5)P2, is reduced significantly ($\sim 90\%$ – Masters et al., 2016), as can be seen in the PI(4,5)P2 scan Fig. 3. At the left of Fig. 4 is a line-scan of PI(4,5)P2 and actin along the yellow dashed line at the 300 s mark of the sequence shown in Fig 3, while a schematic representation of the actin waves is shown at the right. The PI(4,5)P2 density changes abruptly at a "shoulder" at either edge of the wave, at approximately the same position as the outer edge of the actin wave. Note that the yellow dashed line in Fig 3 extends beyond the attached membrane at both edges, which explains the sudden drop of both profiles at the sides.

PIP3 levels are low in resting cells, but increase upon activation of the FcγR 's. Synthesis of PIP3 occurs in two stages, one shortly after engagement of IgG and another which marks the transition from early to late stages of phagocytosis (Beemiller et al., 2010; Zhang et al., 2010). Production of PIP3 in the first stage occurs mainly via activation of PI3K by Cdc42 (Beemiller et al., 2010), whereas the second stage involves positive feedback between PIP3 and the FcγRs. The feedback occurs via the adapter protein Gab2, which upon its PIP3-mediated recruitment to the membrane can attract PI3K to the receptor scaffold, which then activates it (Gu et al., 2003). PIP3 is the target of enzymes such as PTEN and SHIP2. The lipid phosphatase PTEN, which can attach to the membrane at a basal rate and is also recruited by PI(4,5)P2 (Vazquez et al., 2006), lowers PIP3 levels in a global fashion as it does not display enhanced activation at sites of receptor activation (Kamen et al., 2007). Accordingly, PTEN is present uniformly within the actin waves.

The phosphatase SHIP-1, which metabolizes PIP3 to PI(3,4)P2, co-localizes with the FcγRs following their activation (Kamen et al., 2007; Ai et al., 2006), but how this happens is not clear, and SHIP1 is not observed in the actin waves. Instead, the similar phosphatase SHIP2 is observed in a ring-like distribution. However, rather than co-localizing with the actin wave, the ring occurs somewhat closer to the wave center, as shown in Fig. 5. On some occasions the actin waves oscillate in space, and when this happens, the SHIP2 ring-like distribution dynamically follows them. This suggests that SHIP2 may be recruited by an actin adapter protein, as has been observed in other contexts such as in invadopodiums formed by breast cancer cells (Sharma et al., 2013). PI(3,4)P2 does not co-localize with SHIP2 – instead it is enhanced in the back of the actin waves (Masters et al., 2016). The concerted effects of all the enzymes described above does not lead to a fixed distribution of PIP3 within the actin waves - sometimes it shows weak enhancement in the back of the waves and sometimes it localizes preferentially on the actin waves (Masters et al., 2016).

The Rho GTPases Cdc42 and Rac1, which are involved in enzyme activation as described above, and also in actin polymerization (Hoppe and Swanson, 2004; Beemiller et al., 2006), display similar dynamics during phagocytosis. Specifically, Cdc42-GTP is recruited to the FcγRs immediately after their activation, while Rac1-GTP follows shortly after (Hoppe and Swanson, 2004).[5] Active Cdc42 and Rac1 are involved in actin polymerization in this early stage by their activation of N-WASP and WAVE, respectively (Rohatgi et al., 2000; Beemiller et al., 2010; Ikeda, 2017). Once PIP3 reaches a threshold level it attracts Rho GAPS to the membrane, which inactivate Rac1

---

[5] Rac1 activation is PI3K-dependent in some cells. However in Beemiller et al. (2010), LY294002 treatment did not delay Rac1 activation or decrease the magnitude of Rac1 activation, indicating this was not the case for macrophages.
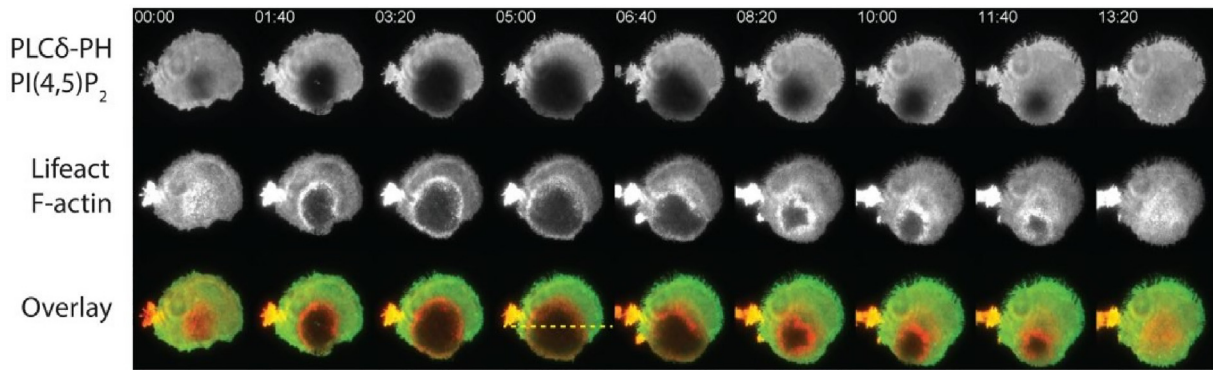
Fig. 3. Dynamics of actin (Lifeact) and PI(4,5)P2 (PLCδ-PH) depletion in the center of a forming wave immediately following a hypotonic shock. The F-actin sequence shows an inital higher level of actin at the center which is followed by a rapid decrease at 100 s, with actin only in the whote ring. The wave grows but eventually collapses and the system returns to a steady state. Reproduced from Masters et al. (2016) with permission.
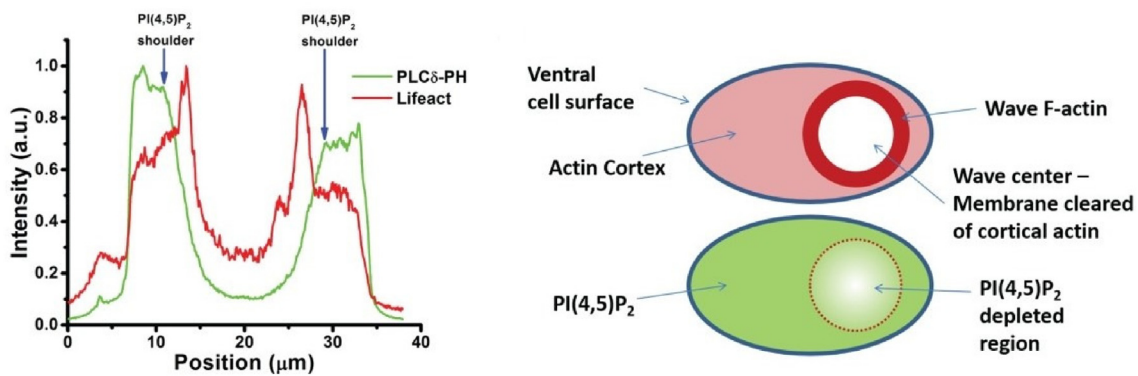

Fig. 4. (Left) Linescan of PI(4,5)P2 (PLCδ-PH) and actin (Lifeact) intensity at 300 s in the sequence shown in 3. The gradient of PI(4,5)P2 density changes abruptly at a "shoulder" at either edge of the wave, at approximately the same position as the outer edge of the actin wave. (Right) A schematic representation of the actin waves. Reproduced from Masters et al. (2016) with permission.
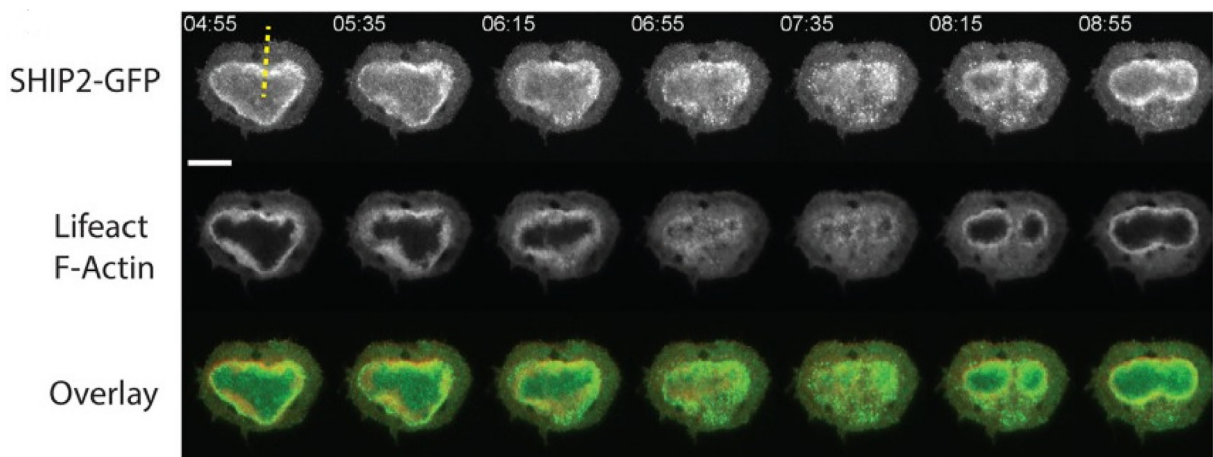
Fig. 5. SHIP2 (SHIP2-GFP) and actin (Lifeact) localization in an oscillating wave. On some occasions the wave sometimes collapses and reforms initially as two separate waves. As these waves expand the boundary between them is annihilated, leading to formation of a single wave. Reproduced from Masters et al. (2016) with permission.

and Cdc42, a requirement for successful phagocytosis of large particles (Schlam et al., 2015). Despite the slight difference in activation kinetics of Rac1 and Cdc42, their role in the initial stages of particle engulfment is functionally redundant. Therefore, in the model described later we include only the dynamics of Cdc42, which displays enhanced localization in the actin waves - and is thus the main driver of actin polymerization.

In summary, imaging of macrophages performing phagocytosis or frustrated phagocytosis has shown that different proteins associate and disassociate from the phagosomal membrane at different times and with different spatial distributions. Experimental results reported in Masters et al. (2016) show that the formation of actin waves is characterized by steep gradients of several phosphoinositides, kinases, phospahatases, and other proteins. Fits to the
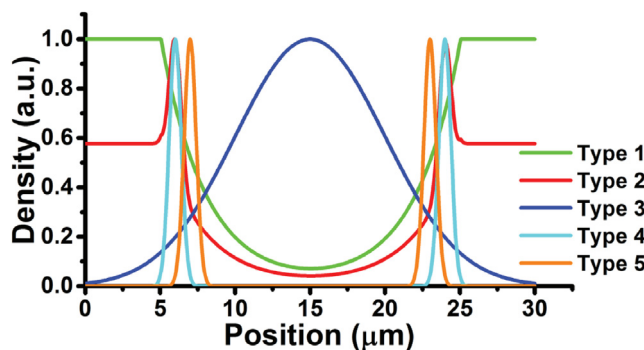
Fig. 6. A summary of the experimental results for lipid and protein distributions in a growing actin wave. Components were classified into 5 types, based on their pattern of reorganization relative to waves: Type 1 - Cortical actin, PI(4,5)P2, PI5K; Type 2 - Total F-actin; Type 3 - PI(3,4)P2, DAG; Type 4 - Branched actin, N-WASP Type 5 - SHIP2. Taken from Masters et al. (2016).

experimental data of different components, each normalized to one, are shown in Fig 6. Each of the five different types represents a class of components characterized as having similar patterns of reorganization in the waves. For example, Type 1 characterizes the distribution of cortical actin, PI(4,5)P2, PI4P5Ks, and others (Masters et al., 2016).

Taken together, the detailed experimental studies of individual steps and the macroscopic observations of the wave behaviors provide the basis for a detailed model that shows how the dynamics of the underlying network can explain the evolution of the actin waves. The experimentally-determined spatio-temporal wave structure described later provides a major test of any model for this system, and will be used in formulating the model for the spatio-temporal dynamics of components that can produce the observed wave structure. The first step in the entire process is receptor activation, and we begin with a discussion of several models concerning how localized receptor activation leads to spatial propagation.

3. Bridging the scales: from receptor activation to particle engulfment

The foregoing shows that activation of the FcγR signal transduction network leads to a sequence of spatial and temporal patterns of actin, phosphoinositides and other associated proteins. However, it is not clear how the components of the network interact to produce the observed patterns. Moreover, the fact that the patterns propagate over large regions of the membrane raises the question of if, and if so, how, receptor activation spreads over the cell surface to produce the actin waves.

Early studies on this - which analyzed bona fide three-dimensional phagocytosis - focused on determining whether particle ingestion follows the trigger model or the zipper model (Griffin, 1974; Griffin, 1975). The former refers to a mode of particle ingestion that is initiated by a localized burst of FcγR activation which, when above a threshold, initiates a cellular response whose magnitude is independent of the signal's intensity and leads to engulfment. The latter postulates that particle engulfment occurs as a spatial sequence of FcγR-IgG interactions, the downstream effect of which induces wrapping of the membrane around the particle. It was shown in (Griffin, 1974) and (Griffin, 1975) that macrophage engagement of particles partially coated with IgG did not extend beyond the opsonized region, which suggests that particle engulfment requires continued FcγR activation at the leading edge. However, this does not necessarily preclude a threshold-like mechanism of phagocytosis initiation.

The authors of Swanson and Hoppe (2004) suggest a mechanism for which the zipper model can explain the sequence of patterns in FcγR-mediated phagocytosis. They hypothesize that the timing of signaling from each receptor could be built into the catalytic reaction rates of the molecules in the FcγR receptor complex. Each new FcγR complex could initiate a sequence of signals whose magnitude and duration depend on catalytic rates for phosphorylation and other modifications or protein–protein interactions. Thus the sequence of spatial and temporal patterns would reflect the changing molecular regulatory networks associated with the FcγR. This mechanism can also serve to provide a qualitative explanation of the actin waves, whereby continued actin polymerization at the leading edge is due to de novo FcγR activation.

This mechanism assumes that the FcγRs signal autonomously and envisions a smooth sequence of FcγR-IgG interactions as a wave progresses. However, results in Zhang et al. (2010) led the authors to suggest a form of FcγR coordination, and they identified a PIP3-dependent threshold which controls progression from early to late signals of phagocytosis and commitment to engulfment, but the mechanism of this coordination has still not been fully explained. In one plausible coordination mechanism by which individual FcγR signals are amplified, signaling is coordinated via the lateral diffusion of the Rho GTPases and phosphoinositides (Swanson and Hoppe, 2004). Specifically, the authors suggest that the diffusion-driven spatial patterns of these molecules would define the sequence of FcγR signaling (Hoppe and Swanson, 2004).

Here we hypothesize that the phosphoinositide microenvironment of an FcγR – specifically the levels of PI(4,5)P2 and PIP3 – determines the downstream effect of receptor activation, by controlling the recruitment of specific enzymes to the surrounding membrane. This hypothesis is reflected in the structure of the signal transduction network given in Fig 2. We lump the signals into two categories: the early PI(4,5)P2-dependent signals and the late PIP3-dependent signals. Thus, for example, in the PI(4,5) P2-dominating early stage of engulfment, the FcγRs receptors would promote responses such as PI5K activation and actin polymerization, which would begin to disappear as PI(4,5)P2 is phosphorylated by PI3K to produce PIP3. Within this framework, the effect of the signaling by an individual FcγR is not autonomously defined by the time elapsed since its activation but is rather defined by its micro-environment.

4. The mathematical model

Details of what a mathematical model of the wave-forming process must explain can be understood by reference to Fig. 6. There one sees that Type 1 and 2 components – cortical actin, PI(4,5)P2, PI5K and total F-actin – are high at the front of the wave as compared with behind it. Type 4 and 5 – branched actin, N-WASP and SHIP2 – exhibit a delta-function-like pulse at the leading edge of the wave, and Type 3 – PI(3,4)P2 and DAG, reach a peak behind the wave. One important and puzzling result shown there is that the SHIP2 waveform and that of its product, PI(3,4)P2, are very different. That of SHIP2 is delta-like and closely follows the N-WASP/branched actin wave, whereas the peak of the PI(3,4)P2 wave occurs far behind the wave front. Other questions that arise in explaining the observations include (i) how do we characterize the functional form of the PIP3-dependent response that controls Cdc42 activation, (ii) what role does membrane diffusion of molecules play, and (iii) how do the activation/inactivation rates balance to self-organize into the observed patterns of phosphoinositides and Rho GTPases, and how do these patterns drive the actin waves?.

The model we develop describes the state of macrophages after they have spread over a glass plate coated with IgG for five minutes. Thus, all biochemical reactions occur on a flat disk which represents the region in contact with the coated glass. We assume that contact of the cell with the glass plate has stabilized and thus there is a basal level of receptor occupation, but this level is insufficient to initiate waves. In the experiments the hypotonic shock increases the cell-plate contact and receptor activation significantly, presumably in a spatially-non-uniform manner, and this leads to wide-spread wave activation. To replicate the effect of the shock computationally we impose a localized Gaussian-like perturbation to the uniform distribution of active FcγRs on a small region of the domain. A key requirement in the development of the network is that the spatio-temporal control and evolution of the various lipids and proteins involved controls actin polymerization - see Section 3 above. Inherent in this assumption is the existence of actin "activator" and actin "inhibitor" sub-networks within the overall FcγR network. A careful look at the biochemistry of phagocytosis described above does indeed suggest that following activation of FcγR's, fast PI(4,5)P2-dependent signals activate actin polymerization and slow PIP3-dependent signals inhibit it. In earlier work on FcγR-mediated phagocytosis a similar structure has been proposed (Beemiller et al., 2010). Details of the observed facts that determine the structure and dynamics of the network, and which are incorporated in the model, are described next, and the governing equations that result follow this.

FcγR activation leads to both PI(4,5)P2 and PIP3 production, albeit on different time scales - with PI(4,5)P2 rising faster than PIP3, hence the color assignment to these species in Fig 2. Specifically, upon FcγR activation, Cdc42 is localized at the membrane and activated. Cdc42 can then attract and activate PI3K and also activate the membrane-attached PI5K, but again, it activates PI5K faster than PI3K. PI5K is localized to the membrane by an electrostatic interaction with it's product PI(4,5)P2, and because the steady state density of PI(4,5)P2 is an order of magnitude higher than that of PIP3 (Olivença et al., 2018), we see high levels of active Cdc42, PI(4,5)P2 production and activation of N-WASP - which ultimately leads to actin production - early following FcγR activation. The ability of the FcγR to localize and activate PI3K also depends on it's product PIP3, which again, is low at steady state. Thus, initially Cdc42 attracts some PI3K which begins to produce PIP3. As the PIP3 levels increase, it simultaneously begins to attract Rho GAPs that deactivate Cdc42, which in turn leads to deactivation of N-WASP and also increases the Fcγ-mediated PI3K activation rate. Thus at later stages, once PIP3 reaches high enough levels, one observes deactivation of Cdc42 and depolymerization of actin (Schlam et al., 2015). As a result of having different processes acting on different time scales, the network can be thought of as three interlinked sub-networks: (i) the fast acting actin-activator component, (ii) the slow acting actin-inhibitor component, and (iii) the actin network itself, which comprises N-WASP and both branched and linear actin, and whose spatio-temporal evolution is controlled by the fast and slow sub-nets (*cf.* Fig. 2). In detail, the model is composed of sixteen variables which together form the smallest network that is capable of reproducing the spatio-temporal evolution of actin waves and their molecular footprint. The top-level controller of the network is the FcγR, immediately downstream of it are the variables activated first in the actin-activator component, which contains: Cdc42, PI5K, PTEN, and PI(4,5)P2, coming later in time are the variables in the actin-inhibitor component: PI3K, PLCγ, PIP3, and DAG. The end result, the actin component, contains the variables: N-WASP, branched actin, linear actin, and monomeric actin. The lipid PI(4)P is incorporated in order to act as the primary source of PI(4,5)P2 production

via PI5K, PI(3,4)P2 and the enzyme SHIP2 is incorporated in order to capture the full molecular footprint of the actin wave.

Not surprisingly, the functional form of the FcγR activating rates plays an important role in determining the wave dynamics. We found that a linear Cdc42 and PI(4,5)P2- dependent PI5K activation rate, coupled with a Hill-function PIP3-dependent PI3K activation leads to the observed pattern of waves. The fact that the FcγR activating rate of PI3K depends on it's own product suggests a Hill-function activation rate, and this assumption is supported by experimental evidence (Gu et al., 2003; Papayannopoulos, 2005).

The role of actin feedback is established, but the precise locus of the feedback is not known. We found that actin feedback on Cdc42 activation does lead to wave formation, but the wave profile does not match that observed in Fig. 6, because this leads to a PI(4,5)P2 wave that doesn't match the observations. Actin feedback on N-WASP activation/activity is supported by ample experimental evidence and it is made particularly clear in (Mullins et al., 2018). We use a Hill coefficient of four for activation in the model, and this is in fact much lower than measured values, which were estimated to be as high as twenty (Papayannopoulos, 2005). This very sharp PI(4,5)P2 activation threshold can explain the abrupt loss of actin in the back of the wave.

In order to simplify the computational model, we assume a quasi-steady-state relationship between the membrane and cytosol concentrations of species that cycle between these domains, which enables us to reduce the problem to a reaction–diffusion system on a disc. A brief analysis developed in the Appendix is used to justify this. Further, we simplify the overall kinetic mechanism by simplifying the description of various steps. These simplifications are implicit in the list of reactions given below. In several cases, such as *fcγ*, we assume a total fixed amount of the component. In other cases. for instance, in reaction (3), Cdc42 is directly activated at a rate proportional to the amount of activated FcγR, which neglects the intermediate binding step involved in the activation. In general, we assume that the local activation rate of any relevant molecule is proportional to the density of the activating molecule - if there is one - and the molecule's local membrane recruitment rate. Depending on the molecule, the local membrane recruitment rate may be a constant basal membrane-binding rate, a function of another molecule - usually a phosphoinositide - or both. We also assume that all active membrane-bound molecules inactivate at a constant rate and detach from the membrane into the cytosol.

To simplify the description of the actin dynamics we have omitted Arp2/3 and assume that branched actin is produced in proportion to the amount of activated N-WASP. A detailed mechanism for branch formation requires many more steps and the inclusion of more molecules in the actin component of the network (Mullins et al., 2018), but here we included only the molecules whose spatio-temporal evolution was analyzed in Masters et al., 2016. Finally, we assume that the total amount of actin monomers is large enough that changes in the monomer level present before contact with the surface is negligible. This is reasonable given that the changes in the actin network are confined to one part of the membrane. The full system of reaction–diffusion equations - which involves 16 variables – is given below. All diffusing species are assumed to satisfy zero-flux conditions on the boundary of the disc, and a full list of the chemical reactions and the 36 parameter values in them is given in Table 1. As will be described in section 5, when parameters were unknown they were chosen so as to ensure that the values of the phosphoinositides coincided with experimental data (Olivença et al., 2018). The steady state values of variables in the model are shown in Table 2 below.

Table 1

Table of reactions and reaction rates. All reactions but 10 and 29 follow mass action kinetics, and for these two the reaction rate is proportional to a function of another molecule with the functional form as indicated. The reaction rate k_{29} is listed as a function of branched actin due to a feedback from branched which enhances the N-WASP activation rate (Mullins et al., 2018). The feedback is incorporated as a smooth Hill-like function (see below) with value 1 at the lower or basal level of branched actin and which increases to 2 with increasing branched actin. The symbol M denotes the unit of density on the membrane in *molecules*/μm^2.

Label and Description	Reaction	Parameter	Value
1. Basal activation of FcγR	$Fc\gamma R \rightarrow Fc\gamma R*$	k_1	$10^{-5}\mu m^{-2} \cdot s^{-1}$
2. Basal inactivation of FcγR	$Fc\gamma R* \rightarrow Fc\gamma R$	k_2	$0.005 s^{-1}$
3. Activation of Cdc42 by FcγR	$Fc\gamma R* + cdc42_c \rightarrow Fc\gamma R* + cdc42_m$	k_3	$321.0667 s^{-1}$
4. Inactivation of Cdc42 by PIP3-recruited GAPs	$cdc42_m + pip3 \rightarrow cdc42_c + pip3$	k_4	$4 \times 10^{-4} M^{-1} \cdot s^{-1}$
5. Basal activation of Cdc42	$cdc42_c \rightarrow cdc42_m$	k_5	$3.2107 M \cdot s^{-1}$
6. Basal inactivation of Cdc42	$cdc42_m \rightarrow cdc42_c$	k_6	$0.2 s^{-1}$
7. Activation of PI5K by Cdc42	$cdc42_m + pi5k_c \rightarrow cdc42_m + pi5k_m$	$k_7 \cdot pi45p2$	$2.005 \times 10^{-5} M^{-1} \cdot s^{-1}$
8. Basal inactivation of PI5K	$pi5k_m \rightarrow pi5k_c$	k_8	$0.1 s^{-1}$
9. Activation of PI3K by Cdc42	$cdc42_m + pi3k_c \rightarrow cdc42_m + pi3k_m$	k_9	$3.2818 \times 10^{-5} s^{-1}$
10. Activation of PI3K by FcγR	$Fc\gamma R* + pi3k_c \rightarrow Fc\gamma R* + pi3k_m$	$k_{10} \cdot \frac{pip3^4}{K_{pip3}^4 + pip3^4}$	$3.6644 s^{-1}$
11. Basal inactivation of PI3K	$pi3k_m \rightarrow pi3k_c$	k_{11}	$0.02 s^{-1}$
12. Activation of PLCγ by FcγR	$Fc\gamma R* + plc\gamma_c \rightarrow Fc\gamma R* + plc\gamma_m$	$k_{12} \cdot pip3$	$1.0565 * 10^{-5} M^{-1} \cdot s^{-1}$
13. Basal inactivation of PLCγ	$plc\gamma_m \rightarrow plc\gamma_c$	k_{13}	$0.02 s^{-1}$
14. Basal activation of PTEN	$pten_c \rightarrow pten_m$	k_{14}	$0.0167 M \cdot s^{-1}$
15. Activation of PTEN by PI(4,5) P2	$pi45p2 + pten_c \rightarrow pi45p2 + pten_m$	k_{15}	$1.6722 \times 10^{-6} s^{-1}$
16. Basal inactivation of PTEN	$pten_m \rightarrow pten_c$	k_{16}	$0.1 s^{-1}$
17. Basal activation of SHIP2	$ship2_c \rightarrow ship2_m$	k_{17}	$0.0016 M \cdot s^{-1}$
18. Activation of SHIP2 via branched actin	$ba + ship2_c \rightarrow ba + ship2_m$	k_{18}	$0.0020 s^{-1}$
19. Basal inactivation of SHIP2	$ship2_m \rightarrow ship2_c$	k_{19}	$0.1 s^{-1}$
20. Basal production of PI(4) P	$\rightarrow pi4p1$	k_{20}	$1 M \cdot s^{-1}$
21. Basal conversion of PI(4,5) P2 to PI(4) P	$pi45p2 \rightarrow pi4p1$	k_{21}	$1.4 s^{-1}$
22. PI5K-mediated production of PI(4,5) P2	$pi5k_m + pi4p1 \rightarrow pi5k_m + pi45p2$	k_{22}	$0.0415 M^{-1} \cdot s^{-1}$
23. PI3K-mediated production of PIP3	$pi3k_m + pi45p2 \rightarrow pi3k_m + pip3$	k_{23}	$0.1714 M^{-1} \cdot s^{-1}$
24. PTEN-mediated production of PI(4,5) P2	$pten_m + pip3 \rightarrow pten_m + pi45p2$	k_{24}	$0.3 M^{-1} \cdot s^{-1}$
25. PLCγ-mediated production of DAG	$plc\gamma_m + pi45p2 \rightarrow plc\gamma_m + dag + ip3$	k_{25}	$0.0379 M^{-1} \cdot s^{-1}$
26. Basal conversion of PI(3,4) P2 to PIP3	$pi34p2 \rightarrow pip3$	k_{26}	$0.1 s^{-1}$
27. SHIP2-mediated production of PI(3,4) P2	$ship2_m + pip3 \rightarrow ship2_m + pi34p2$	k_{27}	$0.3141 M^{-1} \cdot s^{-1}$
28. Basal degradation of DAG	$dag \rightarrow$	k_{28}	$0.1 s^{-1}$
29. Activation of N-WASP by Cdc42	$nwasp_c + cdc42_m \rightarrow nwasp_m + cdc42_m$	$k_{29} \cdot f(ba) \cdot \frac{pi45p2^4}{K_{nwasp}^4 + pi45p2^4}$	$0.0166 s^{-1}$
30. Basal inactivation of N-WASP	$nwasp_m \rightarrow nwasp_c$	k_{30}	$0.1 s^{-1}$
31. Branched actin polymerization	$nwasp_m + ga \rightarrow nwasp_m + ba$	k_{31}	$0.0208 M^{-1} \cdot s^{-1}$
32. Branched actin depolymerization	$ba \rightarrow ga$	k_{32}	$0.1 s^{-1}$
33. Linear actin polymerization	$ga \rightarrow la$	$k_{33} \cdot pi45p2$	$1 \times 10\text{--}5 M^{-1} \cdot s^{-1}$
34. Linear actin depolymerization	$la \rightarrow ga$	k_{34}	$0.1 s^{-1}$

$$\frac{\partial fc\gamma}{\partial t} = k_1 - k_2 \cdot fc\gamma,$$

$$\frac{\partial cdc42_m}{\partial t} = \nabla \cdot (D_{cdc42}(la)\nabla cdc42_m) + k_3 \cdot fc\gamma - k_4 \cdot cdc42_m \cdot pip3 + k_5 - k_6 \cdot cdc42_m,$$

$$\frac{\partial pi5k_m}{\partial t} = \nabla \cdot (D_{pi5k}(la)\nabla pi5k_m) + k_7 \cdot cdc42_m \cdot pi45p2 - k_8 \cdot pi5k_m,$$

$$\frac{\partial pi3k_m}{\partial t} = \nabla \cdot (D_{pi3k}(la)\nabla pi3k_m) + k_9 \cdot cdc42_m + k_{10} \cdot fc\gamma \cdot \frac{pip3^4}{K_{pip3}^4 + pip3^4} - k_{11} \cdot pi3k_m,$$

$$\frac{\partial plc\gamma}{\partial t} = \nabla \cdot (D_{plc\gamma}(la)\nabla plc\gamma) + k_{12} \cdot fc\gamma \cdot pip3 - k_{13} \cdot plc\gamma_m,$$

$$\frac{\partial pten_m}{\partial t} = \nabla \cdot (D_{pten}(la)\nabla pten) + k_{14} + k_{15} \cdot pi45p2 - k_{16} \cdot pten_m,$$

$$\frac{\partial ship2_m}{\partial t} = \nabla \cdot (D_{ship2}(la)\nabla ship2) + k_{17} + k_{18} \cdot ba - k_{19} \cdot ship2_m,$$

$$\frac{\partial pi4p1}{\partial t} = \nabla \cdot (D_{pi4p1}(la)\nabla pi4p1) + k_{20} + k_{21} \cdot pi45p2 - k_{22} \cdot pi5k_m \cdot pi4p1,$$

$$\frac{\partial pi45p2}{\partial t} = \nabla \cdot (D_{pi45p2}(la)\nabla pi45p2) + k_{22} \cdot pi5k_m \cdot pi4p1 - k_{21} \cdot pi45p2 - k_{23} \cdot pi3k_m \cdot pi45p2 + k_{24} \cdot pten_m \cdot pip3 - k_{25} \cdot plc\gamma_m \cdot pi45p2,$$

$$\frac{\partial pip3}{\partial t} = \nabla \cdot (D_{pip3}(la)\nabla pip3) + k_{23} \cdot pi3k_m \cdot pi45p2 - k_{24} \cdot pten_m \cdot pip3 + k_{26} \cdot pi34p2 - k_{27} \cdot ship2_m \cdot pip3,$$

$$\frac{\partial pi34p2}{\partial t} = \nabla \cdot (D_{pi34p2}(la)\nabla pi34p2) + k_{27} \cdot ship2_m \cdot pip3 - k_{26} \cdot pi34p2,$$

$$\frac{\partial dag}{\partial t} = \nabla \cdot (D_{dag}(la)\nabla dag) + k_{25} \cdot plc\gamma_m \cdot pi45p2 - k_{28} \cdot dag,$$

$$\frac{\partial nwasp}{\partial t} = \nabla \cdot (D_{nwasp}(la)\nabla nwasp_m) + k_{29}(ba) \cdot cdc42_m \cdot \frac{pi45p2^4}{K_{nwasp_m}^4 + pi45p2^4} - k_{30} \cdot nwasp_m,$$

$$\frac{\partial ba}{\partial t} = k_{31} \cdot nwasp_m \cdot ga - k_{32} \cdot ba,$$

$$\frac{\partial la}{\partial t} = k_{33} \cdot pi45p2 \cdot ga - k_{34} \cdot la,$$

$$\frac{\partial ga}{\partial t} = \nabla \cdot (D_{ga}\nabla ga) + k_{32} \cdot ba + k_{34} \cdot la - k_{31} \cdot nwasp_m \cdot ga - k_{33} \cdot pi45p2 \cdot ga.$$

Initially we assumed that the diffusion coefficients of membrane-bound species were constant, but we found that the spatial separation between the SHIP2 wave and that of PI(3,4) P2 shown in Fig. 6 could not be reproduced under that assumption. However, it has been shown that the actin cortex can reduce the membrane diffusion coefficient of proteins and phosphoinositides from 5–100 times (Fujiwara, 2002), and therefore the diffusion coefficients of the membrane components were all made a smooth, monotone-decreasing function of the linear actin density. Later we will show computationally and explain why the puzzling dispar-

Table 2
Steady state values.

Molecule	Base steady state SS1	Second steady state SS2	Third steady state SS3
1.Active Fc_γ	0.01 M	0.01 M	0.01 M
2.Cdc42	16.0533 M	16.0533 M	2.8087 M
3. PI5K	32.1153 M	32.1153 M	0.5387 M
4. PI3K	0.0293 M	0.0293 M	1.7450 M
5.PLC_γ	0.0026 M	0.0026 M	0.0275 M
6. PTEN	0.3344 M	0.3344 M	0.1832 M
7.SHIP2	0.0318 M	0.0442 M	0.0159 M
8. PI(4) P	10500 M	10500 M	60050 M
9.PI(3,4) P2	50 M	69.5 M	958.68 M
10.PI(4,5) P2	10000 M	10000 M	5215 M
11.PIP3	500 M	500 M	260.80 M
12. DAG	10 M	10 M	10 M
13.N-WASP	1.6053 M	3.2240 M	0 M
14.Branched actin	0.8027 M	1.4100 M	0 M
15.Linear actin	2.4080 M	2.1059 M	0.4915 M
16.Monomeric actin	2.4080 M	2.1026 M	5.1245 M

ity between the localization of SHIP2 and its product PI(3,4) P2 cannot be captured without this assumption.

5. Parameter sources

Here we discuss the procedure used to estimate the parameters used in simulations of the model equations. Many can be estimated directly from reported biological experiments. Others can be approximated or inferred by combining known basal (steady-state) concentrations with estimates for timescales of down or upregulation in response to a signal. [6] To our knowledge, there is little quantitative information on the deactivation rates of the species in the model. Most of the information that is known about the deactivation rate of one species is on it's speed relative to another species in the model. Thus, in order to populate the deactivation rates of all the species, we opted to choose the deactivation rate of PI5K, k_8, to reflect the time scale within which a wave unfolds in the experimental data and then choose rate values for the other species in the model according to it's speed relative to PI5K - as defined in the signal transduction network shown in Fig. 2. The experimental data in Masters et al. (2016) indicates that after a hypotonic shock waves are formed within 100s, which lead us to estimate $k_8 = 0.1s^{-1}$. Following the experimental data outlined above, we assume that Cdc42 fluctuates at a faster timescale than PI5K, we thus assume k_3 to be two times the deactivation rate of PI5K. As discussed above, it is clear that PI3K and PLCγ - k_{11} and k_{13}, respectively - operate on a slower timescale than PI5K and are thus assumed to be five times smaller than k_8. We further assume the deactivation rate of Fcγ - k_2 - to be two times slower than PI5K. Since it is not clear how PTEN, N-WASP, branched actin, and linear actin and DAG evolve relative to PI5K we assume their deactivation rates - k_{16}, k_{30}, k_{34}, and k_{28}, respectively - are equal to that of PI5K. All other parameters and steady states are chosen so as to balance with the already defined rates and densities as outlined below. The parameter values used in the computations are given in Table 1, and the steady states are given in Table 2.

In order to compute the steady state values from the procedure outlined below we must first determine an estimate for the steady state value of active membrane bound PTEN. To do this, we used the values in Arai et al. (2010), which assumed there is a total concentration of PTEN equal to $0.1\mu M$ in a cell of radius $5\mu M$. As is the case with the deactivation rates, there is little quantitative information on the fraction of membrane bound PTEN molecules relative to those in the cytosol. All that is known is that the levels of membrane bound PTEN are low relative to cytosolic PTEN (Liu

et al., 2018; Vazquez et al., 2006), and we chose the fraction to be 1/20. This is an assumption, however, as will be further described later, we claim that the determining factor of wave formation is that the actin activator portion of the network in Fig. 2, reacts faster to a signal than the inhibitor portion does. This characterizes the ensuing trajectories of the molecules in the model following a perturbation, as they relax back to their initial values - or a different value depending on the size of the perturbation (see Section 6). In this sense, what determines wave formation are not the assumed steady state values of any molecule or group of molecules but, rather, the time profiles following a perturbation of the molecules relative to their initial steady state. Thus, assuming we have a total of 0.1 μM of PTEN in a cell of radius 5 μm and that the steady state density of PTEN on the membrane is a fraction - 1/20 - of the total surface density value, which is defined as the surface density value when all of the available PTEN is attached to the membrane, gives a value of 0.3344 M. We also choose a low density of basal active FcγR of 0.01 M.

Estimates for the density of the various phosphoinositide species in our model - $pi4p1^{ss}, pi45p2^{ss}, pip3^{ss}, pi34p2^{ss}, dag^{ss}$ - can be taken from Olivença et al., 2018. Parameter values for the enzymes PI5K, PLCγ and SHIP2 can be found in Du, 2017, while those for PI3K and PTEN can be found in (Arai et al., 2010). Typically, the parameter values are measured assuming Michealies-Menten kinetics, but since we assume mass action kinetics we choose the catalytic efficiency - defined to be the ratio of the catalytic rate constant over the K_M value - as an approximation to the rate constants: $k_{22}, k_{23}, k_{24}, k_{25}, k_{27}$. The PI(4,5)P2 to PI(4)P decay rate - k_{21} - can be taken from Dawes and Edelstein-Keshet, 2007. While the PIP3 to PI(3,4)P2 decay rate - k_{26} - is chosen to be equal the DAG decay rate - $k_{28} = 0.1s^{-1}$.

With the enzyme reaction rates, the decay rates, the phosphoinositide density values and the steady state value for PTEN, we can estimate the steady state densities of the enzymes - $pi5k_m^{ss}, pi3k_m^{ss}, pten_m^{ss}, plc\gamma_m^{ss}, ship2_m^{ss}$ - by solving for these variables in the steady state equation below.

$$k_{20} + k_{21} \cdot pi45p2^{ss} - k_{22} \cdot pi5k_m^{ss} \cdot pi4p1^{ss} = 0,$$
$$k_{22} \cdot pi5k_m^{ss} \cdot pi4p1^{ss} - k_{21} \cdot pi45p2^{ss} - k_{23} \cdot pi3k_m^{ss} \cdot pi45p2^{ss}$$
$$+ k_{24} \cdot pten_m^{ss} \cdot pip3^{ss} - k_{25} \cdot plc\gamma_m^{ss} \cdot pi45p2^{ss} = 0,$$
$$k_{23} \cdot pi3k_m^{ss} \cdot pi45p2^{ss} - k_{24} \cdot pten_m^{ss} \cdot pip3^{ss} + k_{26} \cdot pi34p2^{ss}$$
$$- k_{27} \cdot ship2_m^{ss} \cdot pip3^{ss} = 0,$$
$$k_{27} \cdot ship2_m^{ss} \cdot pip3^{ss} - k_{26} \cdot pi34p2^{ss} = 0,$$
$$k_{25} \cdot plc\gamma_m^{ss} \cdot pi45p2^{ss} - k_{28} \cdot dag^{ss} = 0.$$

---

[6] Rates and concentrations coming from computational and analytical analysis are reported to four decimal places.

Similarly, in order to compute the rest of the steady state values we must estimate a steady state value for Cdc42. Assuming a concentration of 2.4μM of Cdc42 (Dawes and Edelstein-Keshet, 2007), of which around 1% is active on the membrane (Boulter, 2010), we estimate a steady state density of active Cdc42 of 16.0533 M. Since Cdc42 is the main activator of N-WASP and hence of branched actin as well, we will assume their steady state densities are a fraction - 1/10 and 1/20, respectively - of the steady state density of Cdc42. Finally, we choose the diffusion coefficients D_m, and D_c, to be equal to 0.1$\mu m^2 s^{-1}$, and 10$\mu m^2 s^{-1}$, respectively (Spill, 2016; Dawes and Edelstein-Keshet, 2007). As described above, the value for D_m starts off at this basal value and decreases as a function of linear actin density.

6. Results

6.1. Analysis of the dynamics in spatially-uniform systems

Since there are many variables and parameters in the model, we first consider the dynamics in spatially-uniform systems. The resulting set of ordinary differential equations can be analyzed by standard numerical methods, including stability and bifurcation analysis. The primary objectives are to determine the effect of the feedback of branched actin on the number of steady states, and to analyze the dynamics under various perturbations of FcγR. We begin with SS1 in Table 2, which is obtained by integration of the full PDE system using COMSOL, and as a check, verify that it is indeed a steady state of the ODE system as computed using MATLAB.

The next step is to examine the effect of the feedback of branched actin on the activation of N-WASP by Cdc42 (see reaction 29 in Table 1) via the feedback controller $f(ba)$. As stated in the caption to Table 1, we use a smooth Hill-like function with value 1 at the basal level and 2 at high levels of branched actin. We write this as

$$f(ba) \equiv f(\alpha, \delta) := \frac{1 + 2e^{50(\alpha-\delta)}}{1 + e^{50(\alpha-\delta)}} \tag{1}$$

where α is the ratio of branched actin to its value in SS1. δ is a transition parameter defined by the fact that f takes its midpoint value of 1.5 when $\alpha = \delta$. The nominal value of k_{29} is 0.0166s^{-1}, and $\delta = 1.2$ in the standard parameters (Table 1).

The steady-state values of branched actin as a function of δ and k_{29} are shown in Fig. 7. In the case of the transition value δ we see that small values result in high levels of branched actin, which can

be interpreted as a system in which actin activates nucleating promoting factors much faster than the time-scale on which they decay. At the other extreme, high values in δ will not excite the system fast enough to shift the concentration of branched actin significantly. However, an intermediate region exists in which high and low profiles of branched actin coexist (Fig. 7a). These results are similar to what we observe when varying the parameter k_{29}. We find that small amplitudes of feedback result in low profiles for branched actin, and vice versa (Fig. 7b). We conclude that the choice of parameters in the feedback function affects the number of steady states for the ODE system. Moreover, the existence of multiple steady states suggests the possibility of excitability, in that, starting from one steady state, an appropriate perturbation of one or more species may lead to trajectories that converge to a different steady state.

It is reasonable to define SS1 as the system's unperturbed state based on experimental results, since branched actin is usually at low concentrations. Thus, we investigate the trajectories induced by perturbations in the system at SS1 (Table 2). Based on the experimental data, we expect that the system will shift to different profiles of branched actin under FcγR perturbations. We define a perturbation to a species in our set as a scalar factor multiplying its concentration at SS1. Thus, a perturbation of 1 to any component leaves its concentration unchanged, whereas a factor of 2 doubles its concentration from SS1.

As can be seen in Fig. 8, a series of increasing perturbations from the basal amount of active FcγR, holding PI(4,5)P2 at the steady state, shows that small perturbations return to the stable base steady state SS1, while a slightly higher perturbation in the yellow region leads to a trajectory that converges to the second stable steady state SS2. Finally, large perturbations lead to considerably longer trajectories that return to SS1. These trajectories strongly resemble the dynamics of PI(4,5)P2, PIP3 and actin, wherein a transient increase in PI(4,5)P2 is followed by an increase in PIP3 production which leads to PI(4,5)P2 synthesis and actin depolymerization Fig. 8 **(c)**. Lastly, we note that convergence to a third stable state of the system, which we will refer to as SS3 (see Table 2) requires either large perturbations of PI(4,5)P2 or perturbations of both species. In particular, activation of FcγR alone can not achieve this effect as supported by numerical computations (Figs. 8**(a)** and 9). Perturbations of PI(4,5)P2 result in enhanced debranching activity, which ultimately depolymerizes most of the branched actin structures.

As was described earlier, we hypothesize that the waves are induced by local bursts of FcγR activation at a portion of the

(a)

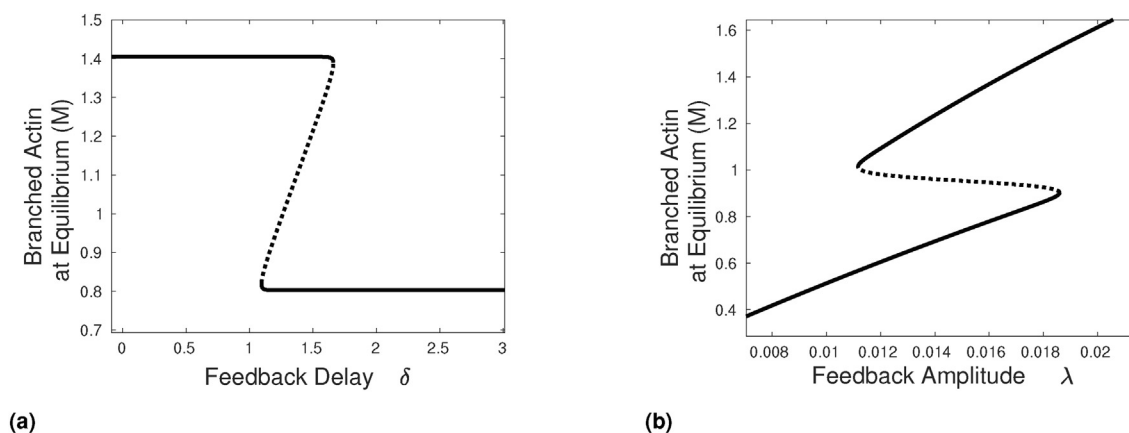
(b)

Fig. 7. The steady-state concentration of branched actin as a function of feedback parameters. Steady states as a function of δ **(a)**, and as a function of k_{29}**(b)**. Solid lines represent stable steady states and dashed lines unstable states. At $\delta = 0$ the branched actin concentration of 1.4 M corresponds to SS2 in the table, and for $\delta > 1.6$M it corresponds to SS1.
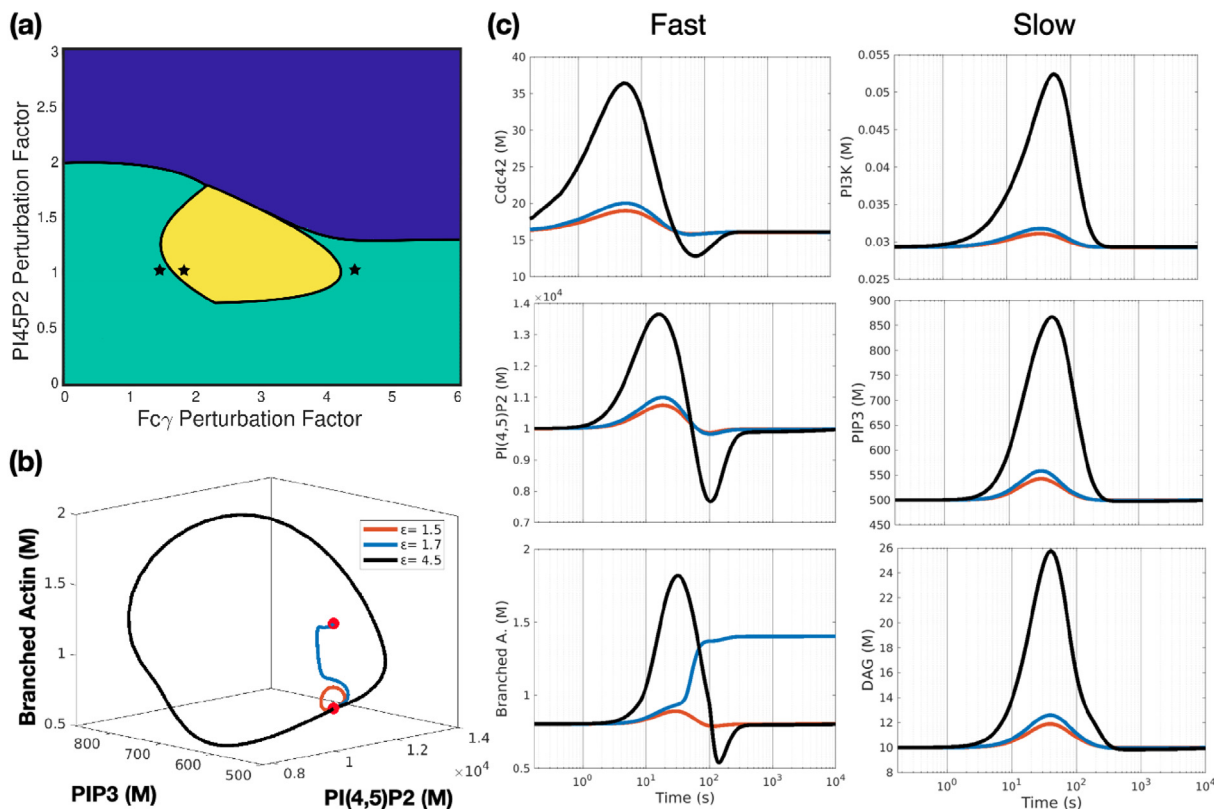
Fig. 8. Effects of perturbations to FcγR. **(a)** Colormap for the convergence of the system with perturbations to PI(4,5)P2 and FcγR. Green regions converge to SS1, yellow regions to SS2, and blue regions to SS3 (Table 2). Stars indicate particular choices used to sample the subsequent figures. **(b)** Trajectories of PIP3, PI(4,5)P2, and branched actin concentrations for particular choices of FcγR perturbation factors. Black = 4.5, blue = 1.7, and orange = 1.5. **(c)** Time dynamics for slow and fast components. of the network.
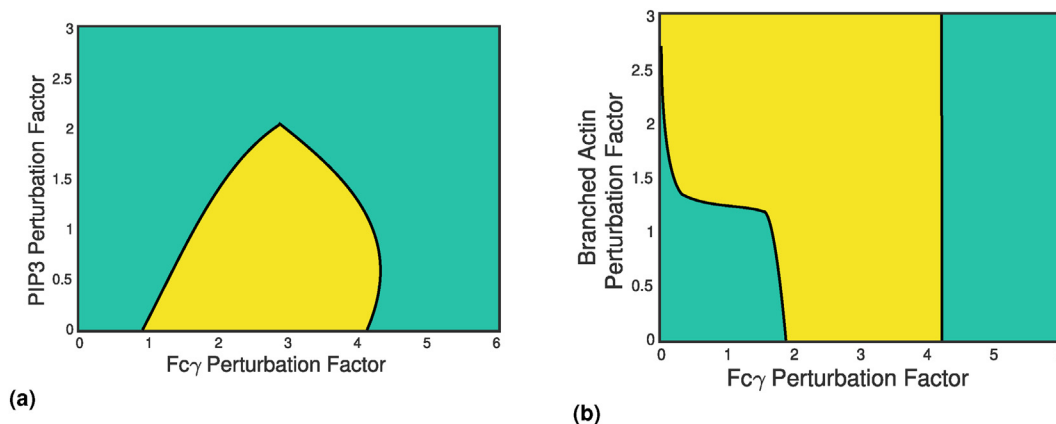
Fig. 9. Convergence of perturbations introduced to SS1. Green regions converge to SS1, yellow regions to SS2.

attached membrane. We thus seek to analyze the terminal steady state that is reached upon perturbations of the basal level of FcγR activation and PI(4,5)P2, PIP3 and branched actin.

6.2. Wave initialization and propagation

To investigate wave initialization and propagation we set all species to their steady-state values throughout the domain – a disk of $20\mu m$ diameter. We then imposed an axisymmetric, localized Gaussian-like perturbation of the density of activated FcγRs, which decays as shown in the table of reactions, at the center of the disk, and solved the full system of reaction–diffusion equations. Fig 10

shows a time sequence of line-scans of Cdc42, PI(4,5)P2, PIP3, and actin, along any diameter, following a transient increase in the steady-state distribution of the FcγRs on a $2\mu m$ interval of the contact surface. The early response at 5 s shows a large increase in Cdc42 and smaller increases in PI(4,5)P2, branched actin, and PIP3. By forty seconds there is a large increase in branched actin, followed by an abrupt dip, and by 160 s, branched actin is depleted to one tenth of it's original density in a 10 μm diameter region, in very good agreement with experimental observations (Masters et al., 2016). At 70 s PIP3 has risen dramatically and one can see the indentation in the actin distribution that later leads to two outgoing waves. In the first 100 s following the wave initialization the
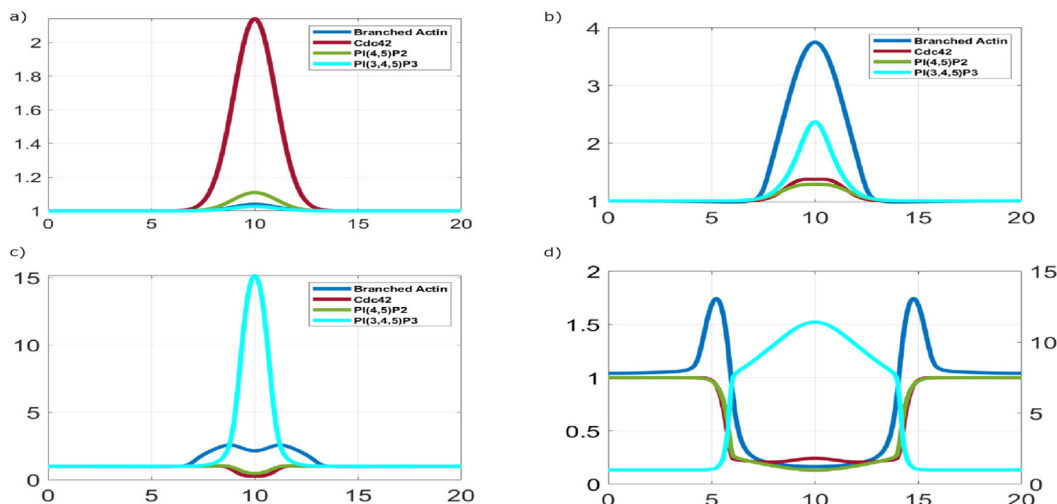
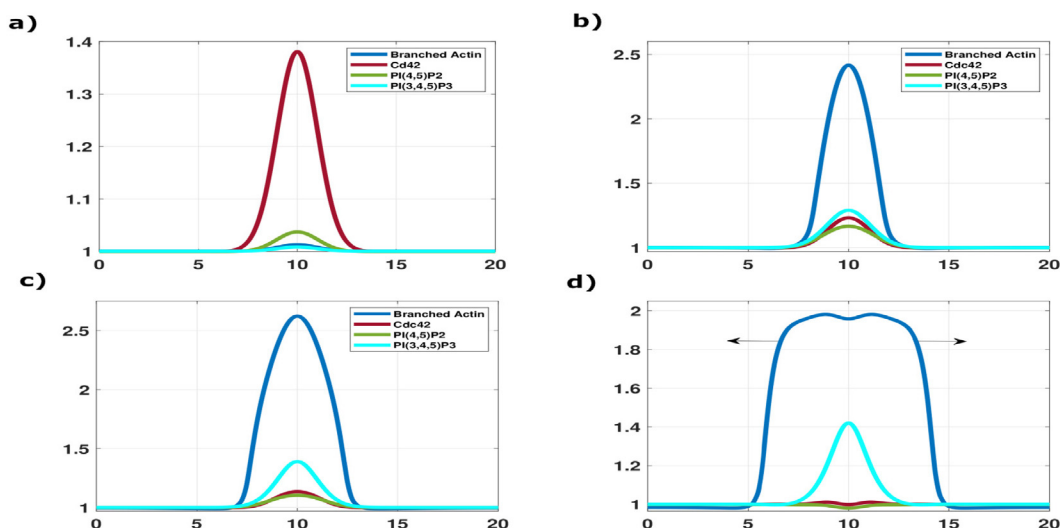**Fig. 10.** Branched actin wave initialization and propagation. Shown are the profiles of branched actin, PI(4,5)P2, Cdc42, and PIP3 at $t = 5$ seconds (a), 40 s (b), 70 s (c) and 180 s (d) after a perturbation. The concentrations are normalized by their original steady state value. The right axis on (d) is for PIP3, which is shown in light cyan. See also video 1 in the supplemental information.

wave travels a distance of $\sim 1.5 \mu$m in 50 s, which translates to a velocity of 0.03 $\mu m/s$, which agrees quite well with the observed speed of 0.04 $\mu m/s$ (Masters et al., 2016).

The transition between the accumulation of actin and the subsequent abrupt dip, which defines the wave profile, can be explained as follows. First, during the initial growth phase, accumulation of branched actin is accelerated by the localized FcγR-mediated surge in Cdc42 activation, which increases PI(4,5)P2 production by PI5K and produces N-WASP activation. These are the early signals mentioned above. The increase in Cdc42 simultaneously increases production of PIP3, and the PIP3 levels will slowly increase until the levels required to fully trigger the FcγRs late signals are reached. At this time (70 s) the PIP3 synthesis rate via PI(4,5)P2 exceeds the net PI(4,5)P2 production rate and leads to a dip in both PI(4,5)P2 and Cdc42, which ultimately causes the abrupt dip in actin. This localized dip in actin defines the back of wave profile. The increased amount of branched actin at the peak of the wave enhances the N-WASP nucleation rate – see reaction 29 in Table 1 – which is critical for propagation of the wave. At

the boundary, the actin wave exhibits a sequence of growth and depolymerization very similar to the dynamics at the wave onset. The actin peak transiently increases and then virtually fades away reaching levels at the order of 10^{-4} of it's initial density at 510 s, and these dynamics are mirrored by linear actin. The complete depolymerization of the actin cortex is followed by a period of relaxation of all components within 2000 s, at which time the system has returned to a steady state – the *base* steady state (SS1) given in Table 2 –that existed prior to stimulation.

We also found that the type of wave that results following a perturbation depends in a threshold manner on the maximum amplitude of the perturbation, which suggests that the system is excitable. The wave dynamics described above arise upon addition of a perturbation with a maximum at the peak of three times the basal density of activated FcγRs. In contrast to this, addition of a spatially-identical perturbation but with a lower peak, equal to the basal amount of activated FcγRs, leads to increased actin polymerization which spreads all the way to the boundary as can be seen in Fig 11. Interestingly, the system does not relax to the base

Fig. 11. Wave initialization and propagation under a reduced stimulus. Shown are the profiles of branched actin, PI(4,5)P2, Cdc42, and PIP3 at $t = 5$ seconds (a), 40 s (b), 70 s (c) and 180 s (d) after a perturbation. The transition wave moves in the direction of the pointed arrows. The concentrations are normalized by the original steady state.
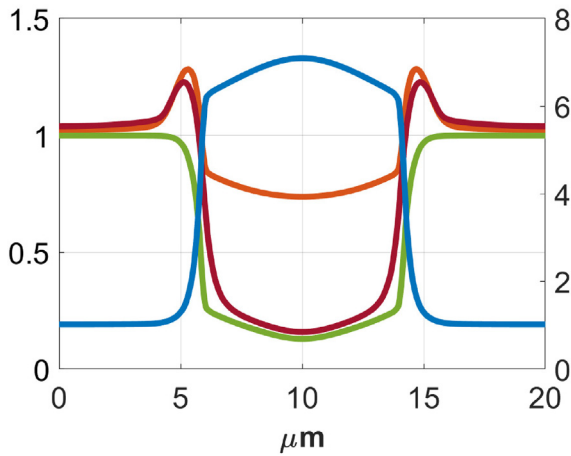
Fig. 12. The spatial profiles of PI(4,5)P2 (Green-Type 1), PI(3,4)P2 (Blue-Type 3), Total F- actin (Red-Type 2), and SHIP2 (Orange-Type 5) 180 s after the applied perturbation. The right axis is for SHIP2. Here, Total F-actin is defined as the sum of branched actin and linear actin. Thus, the red line in this figure plots the distribution of $\frac{ba+la}{ba_{ss}+la_{ss}}$. At the peak of the wave, we have that $\frac{ba}{ba_{ss}} \approx 1.8$ and $\frac{la}{la_{ss}} \approx 1$. Since we know that $\frac{ba_{ss}}{la_{ss}} \approx \frac{1}{3}$ (Fritzsche, 2013), we have that $\frac{ba+la}{ba_{ss}+la_{ss}} \approx \frac{1.8+3}{1+3} = 1.2$, which explains the height difference of the branched actin profile shown in Fig. 10.

steady state, but to a different steady state, – the *second* steady state (SS2) given in Table 2 – in which branched actin is significantly higher than in SS1. Thus the system is at least bistable, but the threshold manifold for wave propagation is complicated, and is not understood at present.

The difference in the types of waves observed can be explained by the distinct peaks of PIP3 production caused by each perturbation. Upon comparison of Figs 10 and 11, one can see that at early times the dynamics of all molecules are similar. In particular, an increase in PIP3 is observed shortly after both perturbations. However, the lower perturbation does not cause an increase in PIP3 synthesis that is strong enough to fully turn on the late PIP3-dependent signals. Thus, in contrast to the case with a higher perturbation, the characteristic initial increase in branched actin is never degraded, and instead spreads across the whole domain, due the actin feedback on N-WASP activation. Experimental evidence for this type of behavior are the results observed in Zhang et al., 2010, wherein FcγR-dependent responses of macrophages to exposure of beads coated with various densities of IgG were measured. In this study, it was shown that phagocytosis of beads with IgG at low density either stalled after making small, actin-rich cups or proceeded to completion at the same rate as phagocytosis of high density IgG beads. The results of our model represent
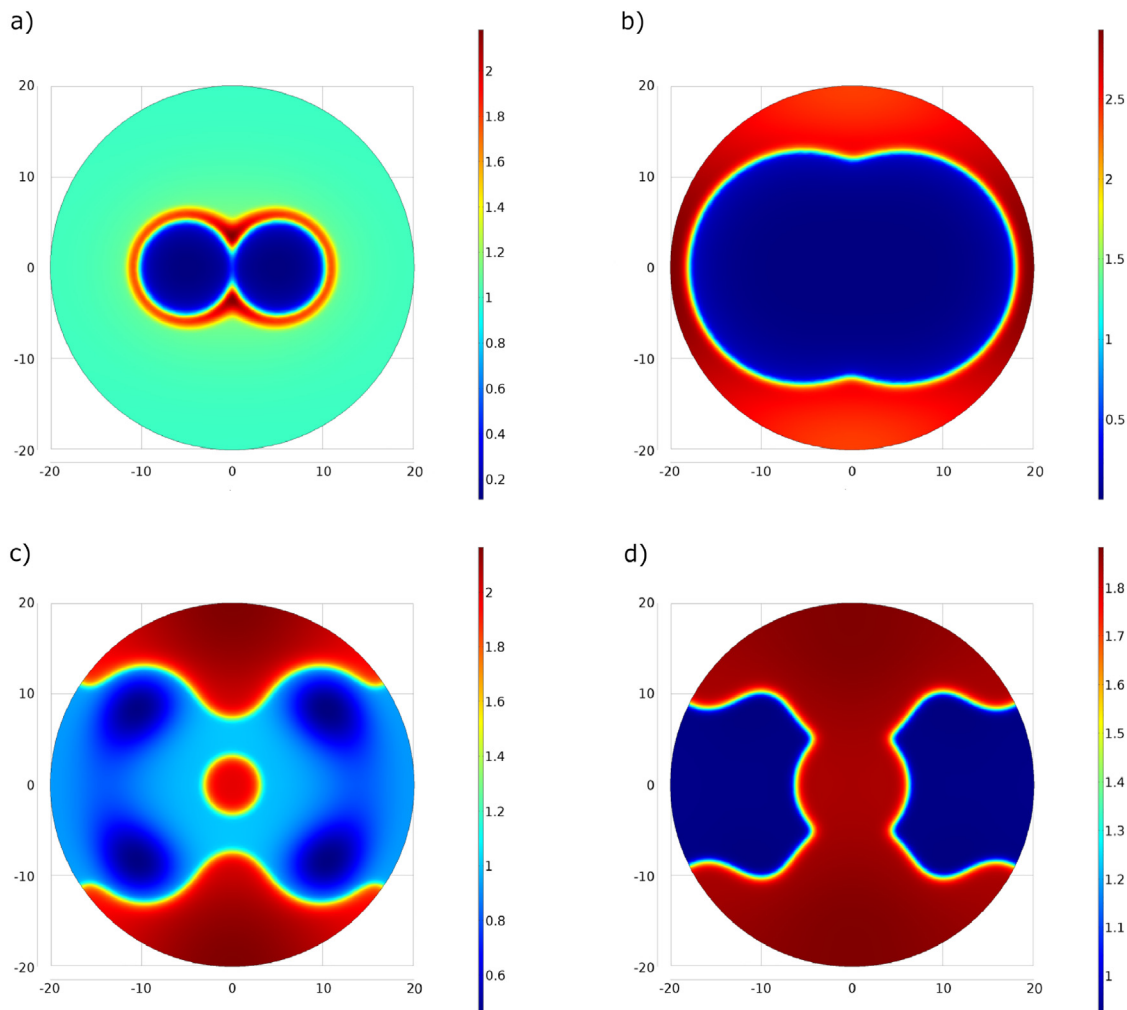
Fig. 13. Two fronts of branched actin colliding in the center of the disk. Figures shown are the distribution profiles at 210 s (a), 500 seconds (b), 1050 s (c) and 1300 s (d). See also video 2 in the supplemental information.

a two-dimensional analogue of the study performed above. Specifically, the actin wave we obtain after a large perturbation is an instance of phagocytosis completion, whereas the transition wave following a low perturbation resembles the stalled actin-rich cup.

The model is also able to capture qualitative details of the experimentally-observed internal structure of fully-established waves, as reflected in the phosphoinositides and other proteins summarized in Fig 6. Figs. 10(D) and 12 show the spatial distributions 180 s after the perturbation of SS1, and a comparison of these figures with Fig. 6 suggests that the model includes all the important components and captures the qualitative space–time behavior of their interactions very well.

6.3. Colliding waves, skewed waves and the long-term dynamics

As was mentioned earlier, the actin waves sometimes showed oscillatory characteristics in which they repeatedly open and close under hypotonic conditions without further perturbation. Furthermore, on some occasions the wave collapses and reforms initially as two separate waves. As these waves expand the boundary between them is eliminated, as can be seen in Fig. 5.

To test whether the model replicates these observations, we initiated waves by applying two perturbations to SS1 equidistant from the center of the disk. In the experiments the cells appear to have spread on a larger region when the colliding waves are observed, and we therefore performed the simulations on a disk of diameter of $40\mu m$. As can be seen in Fig. 13(a), when the two waves collide the boundary between them collapses, in accordance with experimental data and consistent with excitable dynamics.

Following the coalescence of the waves, the composite wave propagates into the remainder of the domain, but the wave front reaches the boundary at different times on the wavefront contour. The wave first reaches the boundary at the right and left edges of the domain, and later along the remainder of the boundary (Fig. 13(b)). At the center of the domain - where the waves collided - the branched actin increases again, as seen in Fig. 13(c), and the center reconnects with the separated portions of the wave at the boundary (Fig. 13(d)), where branched actin is high. Eventually the entire disk relaxes to SS2.

To explain why this happens, in Fig. 14 we show the distribution of PIP3 corresponding to the branched actin distributions shown in Fig. 13. We note that the asymmetric arrival times of the wave at the boundary causes an accumulation of actin above and below the center line - as can be seen 1050 s after initiation of the perturbation (Fig 13). However, due to the increased domain length used in this simulation, PIP3 is not produced at levels high enough to accumulate in these regions, as can be seen in Fig 14 (b) and (c), and thus there is no accumulation of the actin-inhibiting PIP3 at super-threshold levels in these regions. Thus, in this region branched actin is not degraded and relaxes to the second steady state, which then begins to invade the rest of the domain.

We also noticed that on many occasions the waves in experiments emerged in regions that were off-center. We thus computed the dynamics when the perturbation was applied to the left of center. The ensuing dynamics of branched actin and PIP3 are shown in Figs 15 and 16, respectively. The actin wave initialized to the left of center first reaches the boundary, vanishes at this side, but continues traveling towards the right of the domain. As the wave expands
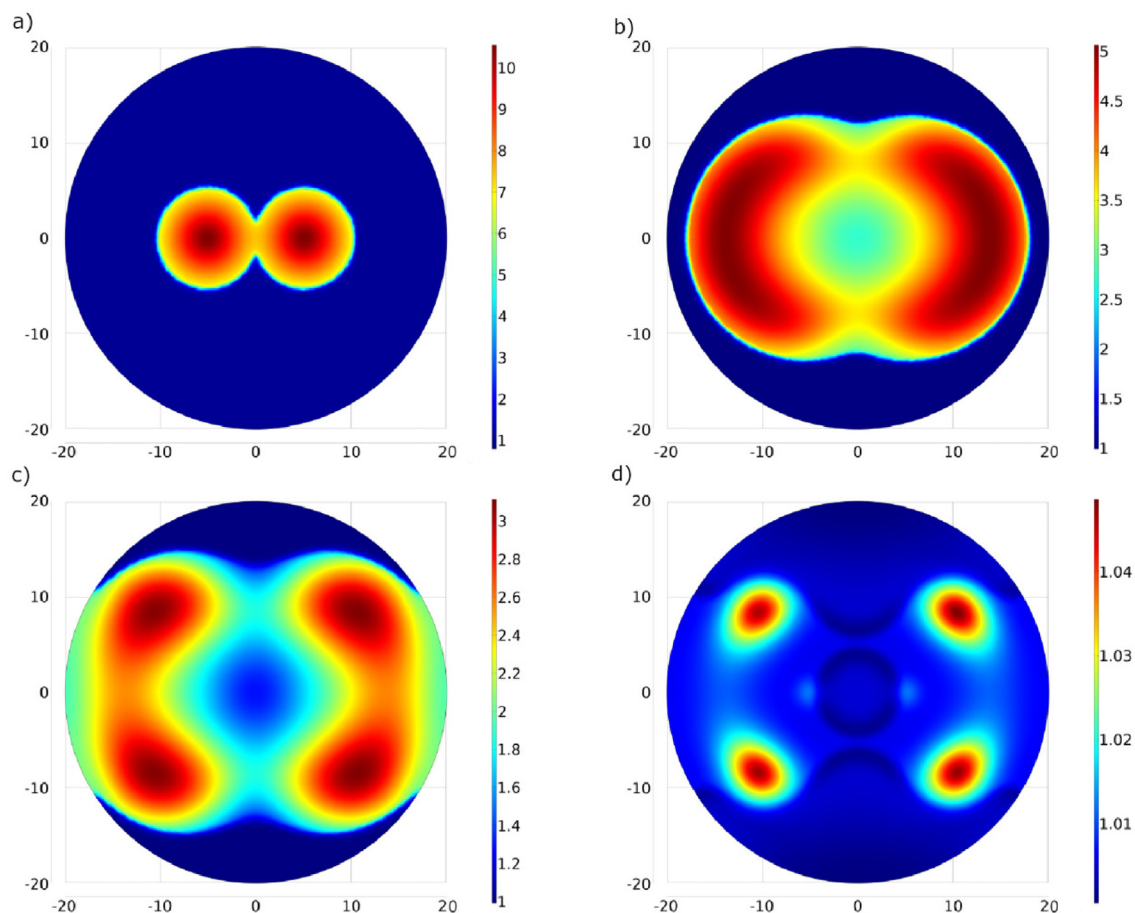

Fig. 14. The distribution of PIP3 at 210 s (a), 500 s (b), 700 s (c), and 1150 s (d) since application of the perturbation that produces the colliding waves.
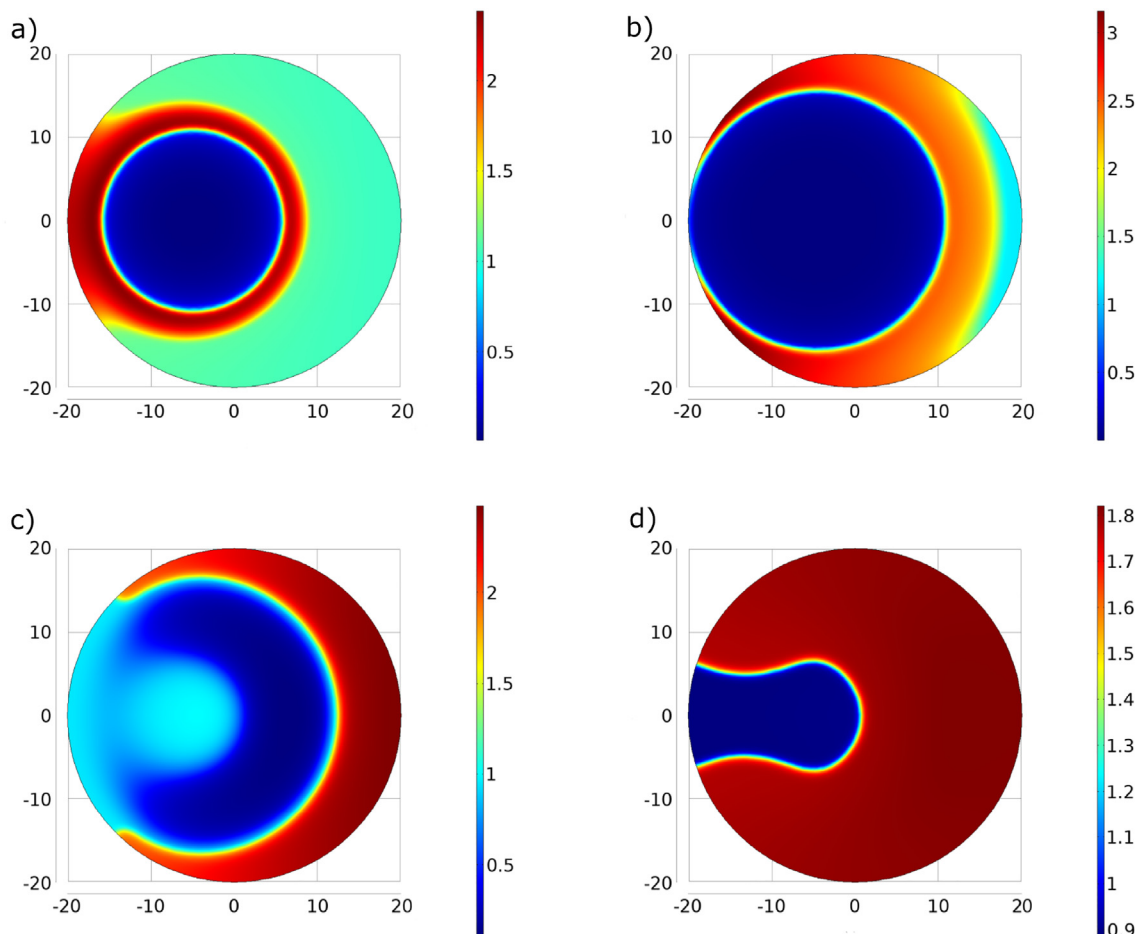
Fig. 15. The actin distributions for a wave initialized to the left of center. Figures shown are the profiles at 400 s (a), 600 s (b), 1000 s (c) and 2000 s (d) post-stimulation. See also video 3 in the supplemental information.
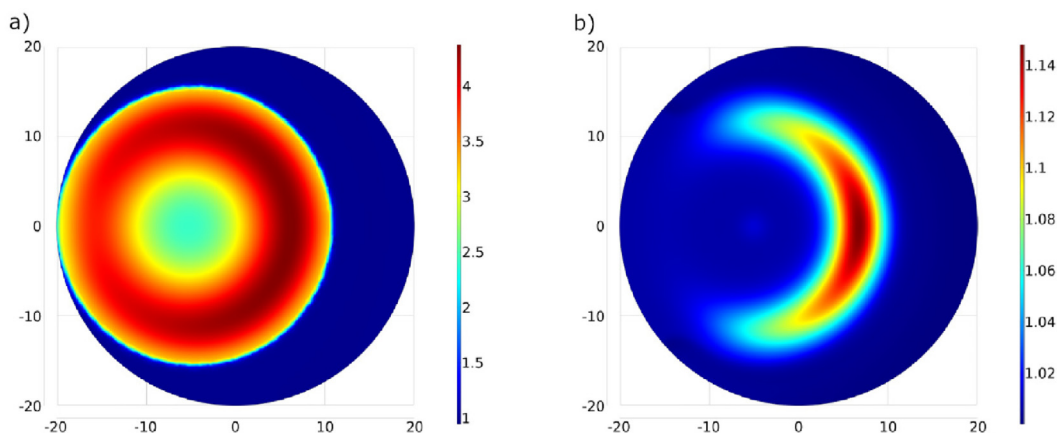

Fig. 16. The distribution of PIP3 at 600 s (a) and 1150 s (b) post-stimulation.

it reaches the right side of the domain but it is not followed by PIP3, again because of the increased domain length. Thus, as described for the colliding waves, the asymmetric wave arrival times to the boundary pushes - in this case - the right edge of the boundary to a state in which branched actin is not degraded and relaxes to the second steady state, which then invades the rest of the domain.

The previous simulations demonstrate that the domain length also plays a role in defining the ensuing long term dynamics fol-

lowing perturbation. This claim is further supported by a reproduction of the computational study presented in Section 6.1, but performed on a larger disk with diameter equal to 40 μm, which displays the same wave dynamics described earlier but later on shows different relaxation dynamics. Specifically, soon after application of a perturbation an actin wave forms which expands towards the domain boundary and is followed by a front of accumulated PIP3. As the wave expands it reaches a critical size whereupon PIP3 begins to degrade at the center of the front and its

propagation begins to slow. When branched actin reaches the border it is not followed by PIP3. Thus, as in the previous two cases mentioned above, branched actin is not degraded at the border and relaxes to the second steady state.

Whether branched actin can relax to a steady state different than the original after a perturbation in experiments is unknown. To check if this is true one can compare the fluorescence intensity of actin just before application of a hypotonic shock with the intensity of actin upon relaxation *i.e.* to compare the intensities measured just before the first frame and at the last frame of Fig 3. However, degradation of PIP3 at the center of a large front has been observed in the context of Dictyostelium discoideum cells (Gerhardt et al., 2014). It can also be observed in the context of frustrated phagocytosis - see the supplementary Fig. 2 in Masters et al., 2016.

6.4. The effect of diffusion in the back of the wave

Earlier we remarked that the model predicts that SHIP2 and its product PI(3,4)P2 do not coincide spatially when the diffusion constants for membrane-bound species are constant over the entire membrane. Specifically, membrane-bound SHIP2 forms its own "wave" situated just behind the actin wave, while PI(3,4)P2 is located further back. Since PI(3,4)P2 is located exactly in the region devoid of cortical actin, we hypothesized that the enhanced diffusion due to cortical depletion might explain the discrepancy in localization. To study this, we compared the phosphoinositide profiles resulting from simulations assuming either a constant or an actin-dependent diffusion coefficient. We introduced the actin dependence of the diffusion coefficients in our model by assuming that they vary as smoothed step functions of the linear actin density. Specifically, the diffusion coefficient starts at 0.01 μm^2/s in normal linear actin levels and increases up to fifty times as linear actin goes down to one fifth of it's original value.

Fig. 17 shows the spatial profiles of branched actin – which doesn't diffuse – and PI(3,4)P2 with and without actin-dependent diffusion coefficients at 250 s post-stimulation. We see that the PI(3,4)P2 profiles of the latter are very distinct from those observed experimentally within the actin waves. In contrast, the distribution profiles of the former agree with experimental evidence. This shows that the increased diffusion in the back of the wave caused by depolymerization of the actin cortex can explain the discrepancy in localization of the enzyme SHIP2 and its product PI(3,4)P2. Fig. 17 also shows that the actin-dependence of diffusion also affects the peak and speed of the branched actin wave. With actin-dependent diffusion the wave speed is 0.03 μm^2/s as was measured above, while the speed of the wave with constant diffusion is lower. At the onset of the wave (100 s), the peak travels at a speed 0.02 μm^2/s for the first 100 s and then begins to decelerate reaching a speed of 0.0012 μm^2/s at 200 s after the initial perturbation. These results justify our use of the actin-dependent diffusion coefficients used in the preceding sections.

7. Discussion

Self-organized actin waves have been observed in various cell types. These include cells such as neurons (Flynn, 2009), *Dictyostelium discoideum* cells (Killich et al., 1994; Asano et al., 2008), leukocytes (Weiner et al., 2007), fibroblasts (Vicker, 2002), melanoma cells (Case, 2011), osteocarcoma cells (Case, 2011), keratocytes (Barnhart, 2011), oocytes (Bement, 2015), and embryos (Bement, 2015). These actin waves are believed to play a role in intracellular transport, cell protrusion, polarization and migration (Inagaki and Katsuno, 2017). In the absence of directional signals, the competition between the Rho and Rac
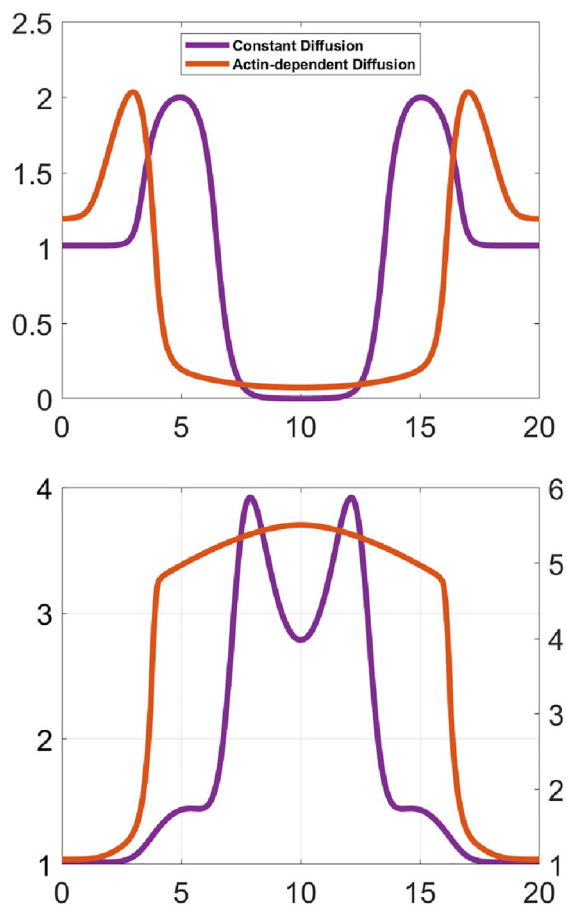

Fig. 17. Comparison of branched actin (top) and PI(3,4) P2 (bottom) with (orange) and without (purple) actin-dependent diffusion constants behind the wave. The profiles are shown at 250 s post-stimulation.

pathways in Dictyostelium discoideum cells and neutrophils leads to complex patterns of traveling actin waves in the cortex in both cell types (Asano et al., 2008; Weiner et al., 2007; Bretschneider et al., 2009; Schroth-Diez et al., 2009; Gerisch et al., 2012). These waves arise at the boundary between domains of high and low PIP3 levels after treatment with latrunculin, which inhibits actin polymerization and annihilates the cortex. The waves are typically closed and of varying shape, and they propagate by treadmilling, as shown by actin recovery after bleaching (Gerisch, 2010). Myosin-IB, which links the actin network to the membrane (Dai et al., 1999), is found at the front of a wave, and the Arp2/3 complex and a dense dendritic network are found throughout the wave. Coronin, which inhibits filament nucleation and indirectly regulates cofilin activity via dephosphorylation(Cai et al., 2007), and cortexillin, which organizes actin filaments into anti-parallel bundles, are found where PIP3 is low.

In this paper we developed a model of experimentally-observed actin waves in frustrated phagocytosis. The model incorporates the intracellular dynamics of Rho GTPases, phosphoinositides, nucleation promoting factors, and actin monomers, and provides insight into the wave initiation and propagation mechanism. The computational results show that a sufficiently-large localized transient increase in FcγR activation can lead to a super-threshold level of PIP3 and wave initiation. The threshold effect has been observed experimentally in studies of phagocytosis (Zhang et al., 2010), and it was postulated that a feedback loop that enhances N-WASP activation propagates the wave outward. Our model, which is the first mechanistic model of the signaling in FcγR-mediated

actin waves, includes a feedback effect of actin on N-WASP (*cf.* FIg. 2). Our results provide further evidence that FcγRs coordinate to bridge the scales and shows that they can do so via lateral diffusion of the Rho GTPases and phosphoinositides involved. We also show that the *de novo* FcγR activation at the leading edge of the wave is not required for wave propagation.

Existing models of actin waves rely heavily on the existence of generic activation and inhibition feedbacks and on the diffusion of actin (Bernitt et al., 2017 and the references in Inagaki and Katsuno, 2017; Pal et al., 2019). While such models give a very high level description of wave behavior, they provide no insight into the identity of either the interacting molecules or the nature of their reactions, which compromises their utility in characterizing the mechanism underlying the actin waves. Moreover, since the actin network is highly interconnected it is probable that the effective diffusion of the structure will be negligible. Here, by developing a model that incorporates the essential molecules and their experimentally-verified interactions in the underlying cellular process, we obtain a more realistic description of the actin waves - both at the qualitative high level and at the level of the molecular footprint of the waves. A key difference with more detailed earlier models of actin waves, which were made for waves observed in *Dictyostelium discoideum*, is that there PIP3 plays a role in promoting actin polymerization. In the context of FcγR-mediated phagocytosis, however, PIP3 plays an actin inhibiting role. Moreover, actin does not directly feed back into further production of PIP3. Thus the internal structure of the waves is quite different in the two systems.

As explained above, our approach is able to uncover networks capable of producing waves of different shapes and propagation dynamics than the well-known traveling wave pulses or traveling wave fronts. This expands our understanding of the diversity of wave-producing mechanisms and avoids the over-classification of the plethora of experimentally-observed actin waves. For example, the authors of Masters et al. (2016) assert that the actin waves are characteristic of a bi-stable traveling wave front at the boundary between the regions of membrane containing and lacking cortical actin. And indeed, an examination of the profiles in Fig. 6, shows that the concentrated actin profile does resemble one that would result from a bi-stable system. However, if the actin waves are *bona fide* traveling wave fronts, than the molecules in its molecular footprint should also follow the same dynamics. Thus, the profile of the actin favorable PI(4,5)P2 should resemble that of actin, while the actin-inhibiting PIP3 should resemble an upside down version of the actin profile, but Fig. 6 shows that this is not the case. Our model shows that the reality of the evolving wave structure following a perturbation of the active FcγRs is much more complicated. A qualitative description of actin waves was recently proposed in Pal et al. (2019), and here we go several steps further to provide a full description of the components and delineate the architecture of both the FcγR signal transduction network and the cytoskeletal network. The latter is not done in complete detail, because a more detailed model involves numerous other factors (Bieling et al., 2018; Mullins et al., 2018).

Our model also provides insight into the kinetics of the local membrane recruitment rate of important enzymes such as PI5K and PI3K during phagocytosis. Indeed, previous studies have demonstrated that PI(4,5)P2 and PIP3 are involved in the membrane recruitment of PI5K and PI3K, respectively (Gu et al., 2003; Fairn et al., 2009), but the functional forms that correctly approximate the recruitment rates remain unkown. The fact that PI3K recruitment, following FcγR activation, requires its own product suggests that the functional form is a Hill function of PIP3, and here we show that this, and a PI(4,5)P2-dependent linear rate for PI5K, can produce the actin waves. The authors of Masters et al. (2016) also suggest that there is an unknown feedback from actin to the

phosphoinositide system. We speculated that this feedback might be the driver of the actin waves. One of the molecules that showed enhanced activation within the actin wave is the Rho-GTPase, Cdc42. We thus performed some additional simulations wherein the occurence of branched actin enhanced the basal activation rate of Cdc42. Interestingly, the simulations showed that this feedback also produces actin waves. However, the arrangement of the other molecules within the wave did not coincide with experimental data. Specifically, the higher activation of Cdc42 on the actin wave led to the production of additional PI(4,5)P2.

Many aspects of both the experimental observations of phagocytosis and the model developed here require far more investigation. For example, further work is needed to understand the threshold behavior in the system, and in particular, whether waves can be triggered by perturbation of other species. Another aspect that should be addressed concerns a sensitivity analysis to identify the most relevant parameters in the model that drive wave formation, but the large number of parameters makes this a major undertaking for the following reasons. As we emphasize at several points in the manuscript, our objective is to explain the spatio-temporal structure of the observed waves. Therefore, standard methods used for sensitivity analysis may not be appropriate. On the one hand, sensitivity analysis of only the local dynamics will remove the effect of diffusion, which plays a major role in determining the structure of the waves. On the other, variance-based sensitivities are dependent on the choice of an objective functional which, given the transient nature of the waves, is not clearly identifiable. Additionally, such computations require a heuristic estimate of $1000(k+2)$ model runs for convergence - with k being the number of parameters to inspect - which is beyond our computational capacity. Similarly, spatio-temporal sensitivity analysis methods will require excessive computational resources. Instead, we argue that robustness of wave formation is dependent more on how fast the actin activator component of the network is relative to the inhibitor, rather than on any one specific parameter (Koda et al., 1979; Barnhart, 2017). To demonstrate this we performed a simulation wherein all the parameters are calibrated with the same set of known data points and using the same procedure outlined in the manuscript, but with the assumption that the kinetics of both the actin activator and inhibitor evolve at the same speed. The contrasting dynamics are displayed in Fig. 18 - see also Video 4 in the supplementary data. In the left panel, we see the dynamics under the original time scales, which displays branched actin traveling from the center towards the domain ends following a perturbation at the center of the domain. However, in the right panel - which depicts the perturbed time scales - branched actin accumulates initially at the center but then quickly relaxes back towards the original steady state. The transient accumulation of branched actin at the boundary - seen in both cases - is an effect of the no-flux boundary condition which allows for the continued polymerization of branched actin due to the positive feedback embedded in the actin network, once either the fully formed wave or the small traces of actin reach the boundary in the unperturbed or perturbed case, respectively. In both cases, actin relaxes back to the original steady state once PIP3 arrives at the boundary - see Fig. 19 in the supplementary data.

Thus, it can be surmised that robust wave formation will occur following a perturbation so long as the actin activator component of the network is faster than the inhibitor. Additionally, we performed simulations wherein we varied the values of a small set of parameters that we deem essential -the velocities and activation rates of all involved enzymes- and analyzed the effects on the dynamics following perturbation. We found that variations of one of these parameters of up to one order of magnitude - while leaving the rest fixed - does not significantly affect wave formation
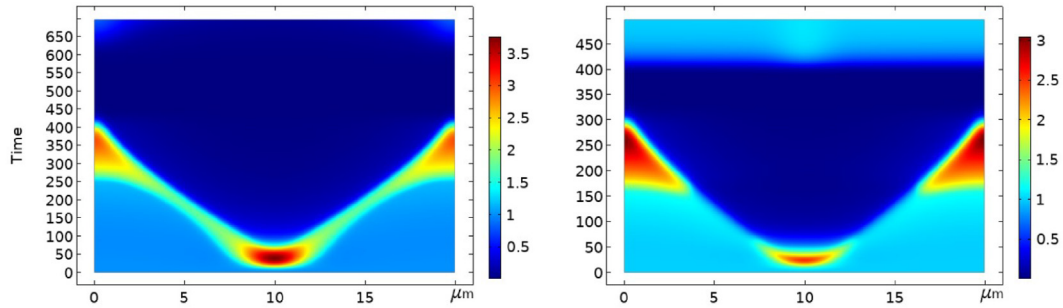
Fig. 18. The evolution of branched actin on the horizontal cross-section through the center of the domain, post-stimulation, under the original time scales - left - and the perturbed time scales - right.

after the applied perturbation. The potential significance of mechanical feedback as a regulator of cytoskeletal dynamics and hence of the waves, should be studied. In our model, we focused on the activation of the FcγR's as the underlying driver of wave initialization, but mechanical feedback may play a significant role in wave generation, as has been observed for waves arising in other contexts such as cell adhesion (Singh and Insall, 2021; Katsumi, 2004). Conversely, mechanical feedback may be negligible for wave propagation, at least on flat surfaces as seen in *Dictyostelium discoideum* cells, where actin waves propagate at constant speeds across the entirety of the membrane even in abnormally enlarged cells (Gerhardt et al., 2014). Moreover, the pathways activated during wave initialization in contexts other than frustrated phagocytosis may vary significantly depending on the cell type (Barger, 2019) and hence, may not be relevant to our case. Finally, a larger problem centers on coupling the biochemical model developed here, with a mechanical model of the cytoskeleton capable of capturing the membrane-cytoskeleton mechanical interactions in phagocytosis. Such a model would be complex, but could help to dissect the underlying biochemical and mechanical mechanisms underlying phagocytosis, and contribute to understanding other types of endocytosis such clathrin-mediated endocytosis, macropinocytosis and dorsal ruffles.

Funding

Declaration of Competing Interest

The authors declare that they have no known competing financial interests or personal relationships that could have appeared to influence the work reported in this paper.

Appendix A. Dimensional analysis

Since all the reactions occur on the membrane attached to the glass plate, we assume that the equations hold on a disk of radius R and thickness h such that $R \gg h$. To avoid the complication of distinct concentration units for the molecules on the membrane versus those in the cytosol, we will consider the cytosolic protein levels as effective mean concentrations within a vertical column though the cell, assumed to be of constant thickness (Spill, 2016). This is reasonable because the vertical dependence of the cytosolic distribution is weak due to the fact that $R \gg h$ (Saltelli, 2008). Since the molecules cannot diffuse out of the cell, we impose no-flux condi-

tions at the boundary. All molecules considered in our model except the phosphoinositides are constantly interchanging between an inactive cytosolic form and a membrane-bound active form. Thus, they all follow the following generic system of equations. Let the variables P_m, and P_c denote the membrane and cytosolic distributions of a molecule in the system respectively, then the following equation holds:

$$\frac{\partial P_m}{\partial t} = \nabla \cdot (D_m \nabla P_m) + k_1 \cdot P_c - k_2 \cdot P_m,$$

$$\frac{\partial P_c}{\partial t} = \nabla \cdot (D_c \nabla P_c) + k_2 \cdot P_m - k_1 \cdot P_c,$$

where k_1 and k_2 are the membrane attachment and detachment rates, respectively. To non-dimensionalize the system we choose $x = R \cdot x'$ and $t = \frac{R^2}{D_m} \cdot t'$ to get:

$$\frac{\partial P_m}{\partial t'} = \nabla \cdot (\nabla P_m) + \frac{R^2}{D_m} \cdot (k_1 \cdot P_c - k_2 \cdot P_m),$$

$$\frac{D_m}{D_c} \cdot \frac{\partial P_c}{\partial t'} = \nabla \cdot (\nabla P_c) + \frac{R^2}{D_c} \cdot (k_2 \cdot P_m - k_1 \cdot P_c).$$

In order to reduce the system of equations as much as possible, we make the reasonable assumptions that $\frac{D_m}{D_c} = O(\epsilon)$ and k_1 and k_2 are big enough so that $\frac{R^2 \cdot k_1}{D_c}, \frac{R^2 \cdot k_2}{D_c} = O(1)$. It will follow then that $\frac{D_m}{R^2 k_1} = O(\varepsilon)$, and $\frac{k_2}{k_1} = O(1)$. Rearranging the equations above we have:

$$\frac{D_m}{R^2 k_1} \frac{\partial P_m}{\partial t'} = \frac{D_m}{R^2 k_1} \nabla \cdot (\nabla P_m) + \left(P_c - \frac{k_2}{k_1} \cdot P_m \right),$$

$$\frac{D_m}{D_c} \cdot \frac{\partial P_c}{\partial t'} = \nabla \cdot (\nabla P_c) + \frac{R^2 k_1}{D_c} \cdot \left(\frac{k_2}{k_1} \cdot P_m - \cdot P_c \right).$$

Therefore, on the fast time scale $t' = O(1)$ we have

$$0 = P_c - \frac{k_2}{k_1} \cdot P_m,$$

$$0 = \nabla \cdot (\nabla P_c) + \frac{R^2 k_1}{D_c} \cdot \left(\frac{k_2}{k_1} \cdot P_m - \cdot P_c \right).$$

Thus, $\nabla \cdot (\nabla P_c) = 0$ and we conclude that P_c is spatially homogeneous. Therefore, we are left with the $O(\varepsilon)$ terms in the equations; namely,

$$\frac{\partial P_m}{\partial t'} = \nabla \cdot (\nabla P_m) \text{ and } \frac{dP_c}{dt'} = 0.$$

With P_c being spatially homogeneous at this time-scale it follows that P_c is constant in time. Moreover, if we assume that the kinetic reactions of the membrane occur at the slower timescale $t' = O(\varepsilon)$

$$\frac{\partial P_m}{\partial t'} = \nabla \cdot (\nabla P_m) + \sum_{i \in I} f_i$$

where $\sum_{i \in I} f_i$ represents the set of chemical reactions at the membrane, allowing us to keep track of only the membrane-bound active form. The evolution equations were solved numerically using COMSOL.

Appendix B. Supplementary data

Supplementary data associated with this article can be found, in the online version, at https://doi.org/10.1016/j.jtbi.2021.110764.

References

Ai, J., Maturu, A., Johnson, W., Wang, Y., Marsh, C.B., Tridandapani, S., 2006. The inositol phosphatase SHIP-2 down-regulates FcγR-mediated phagocytosis in murine macrophages independently of SHIP-1. Blood. 107 (2), 813–820.

Allard, Jun, Mogilner, Alex, 2013. Traveling waves in actin dynamics and cell motility. Current Opinion Cell Biol. 25 (1), 107–115.

Arai, Y., Shibata, T., Matsuoka, S., Sato, M.J., Yanagida, T., Ueda, M., 2010. Self-organization of the phosphatidylinositol lipids signaling system for random cell migration. Proc. Natl. Acad. Sci. USA 107 (27), 12399–12404.

Asano, Y., Nagasaki, A., Uyeda, T.Q., 2008. Correlated waves of actin filaments and PIP3 in Dictyostelium cells. Cell Motility Cytoskeleton 65 (12), 923–934.

Asano, Y., Nagasaki, A., Uyeda, T.Q.P., 2008. Correlated waves of actin filaments and PIP3 in Dictyostelium cells. Cell Motility Cytoskeleton 65 (12), 923–934.

Barger, Sarah R et al., 2019. Membrane-cytoskeletal crosstalk mediated by myosin-I regulates adhesion turnover during phagocytosis. Nature Commun. 10 (1), 1–18.

Barnhart, E.L. et al., 2011. An adhesion-dependent switch between mechanisms that determine motile cell shape. PLoS Biol. 9.

Barnhart, Erin L. et al., 2017. Adhesion-dependent wave generation in crawling cells. Curr. Biol. 27 (1), 27–38.

Beemiller, P., Hoppe, A.D., Swanson, J.A.A., 2006. phosphatidylinositol-3-kinase-dependent signal transition regulates ARF1 and ARF6 during Fc<texmath type="inline">gamma </texmath> receptor-mediated phagocytosis. PLoS Biol. 4 (6). e162.

Beemiller, P., Zhang, Y., Mohan, S., Levinsohn, E., Gaeta, I., Hoppe, A.D., et al., 2010. A Cdc42 activation cycle coordinated by PI 3-kinase during Fc receptor-mediated phagocytosis. Mol. Biol. Cell. 21 (3), 470–480.

Bement, W.M. et al., 2015. Activator–inhibitor coupling between Rho signalling and actin assembly makes the cell cortex an excitable medium. Nat. 17, 1471–1483.

Bernitt, E., Döbereiner, H.G., Gov, N.S., Yochelis, A., 2017. Fronts and waves of actin polymerization in a bistability-based mechanism of circular dorsal ruffles. Nature Commun. 8 (1), 1–8.

Beta, C., Gov, N.S., Yochelis, A., 2020. Why a large-scale mode can be essential for understanding intracellular actin waves. Cells. 9 (6), 1533.

Bieling, P., Hansen, S.D., Akin, O., Hayden, C.C., Fletcher, D.A., Mullins, R.D., et al., 2018. WH2 and proline-rich domains of WASP-family proteins collaborate to accelerate actin filament elongation. EMBO J. 37 (1), 102–121.

Bohdanowicz, M., Balkin, D.M., De Camilli, P., Grinstein, S., 2012. Recruitment of OCRL and Inpp5B to phagosomes by Rab5 and APPL1 depletes phosphoinositides and attenuates Akt signaling. Mol. Biol. Cell. 23 (1), 176–187.

Botelho, R.J. et al., 2000. Localized biphasic changes in phosphatidylinositol-4, 5-bisphosphate at sites of phagocytosis. J Cell Biology. 151 (7), 1353–1368.

Boulter, E. et al., 2010. Regulation of Rho GTPase crosstalk, degradation and activity by RhoGDI1. Nature Cell Biol. 12, 5.

Bretschneider, T., Anderson, K., Ecke, M., Müller-Taubenberger, A., Schroth-Diez, B., Ishikawa-Ankerhold, H.C., et al., 2009. The three-dimensional dynamics of actin waves, a model of cytoskeletal self-organization. Biophys. J. 96 (7), 2888–2900.

Buracco S., Claydon S., Insall R. Control of actin dynamics during cell motility. F1000Research. 2019;8..

Cai, L., Marshall, T.W., Uetrecht, A.C., Schafer, D.A., Bear, J.E., 2007. Coronin 1B coordinates Arp2/3 complex and cofilin activities at the leading edge. Cell. 128, 915–929.

Case, L.B. et al., 2011. Adhesive F-actin waves: a novel integrin-mediated adhesion complex coupled to ventral actin polymerization. PLoS One. 6.

Cheng, Y., Felix, B., Othmer, H.G., 2020. The roles of signaling in cytoskeletal changes, random movement, direction-sensing and polarization of eukaryotic cells. Cells 9 (6), 1437.

Cherfils, J., Zeghouf, M., 2013. Regulation of small gtpases by gefs, gaps, and gdis. Physiol. Rev. 93 (1), 269–309.

Dai, J., Ting-Beall, H.P., Hochmuth, R.M., Sheetz, M.P., Titus, M.A., 1999. Myosin I contributes to the generation of resting cortical tension. Biophys. J. 77 (2), 1168–1176.

Dawes, A.T., Edelstein-Keshet, L., 2007. Phosphoinositides and Rho proteins spatially regulate actin polymerization to initiate and maintain directed movement in a one-dimensional model of a motile cell. Biophys. J. 92 (3), 744–768.

Du, W. et al., 2017. Effective combination therapies for B-cell lymphoma predicted by a virtual disease model. Cancer Res. 77 (8), 1818–1830.

Fairn, G.D., Ogata, K., Botelho, R.J., Stahl, P.D., Anderson, R.A., De Camilli, P., et al., 2009. An electrostatic switch displaces phosphatidylinositol phosphate kinases from the membrane during phagocytosis. J Cell Biol. 187 (5), 701–714.

Falasca, M., Logan, S., Lehto, V., Baccante, G., Lemmon, M., Schlessinger, J., 1998. Activation of phospholipase Cγ by PI 3-kinase-induced PH domain-mediated membrane targeting. EMBO J. 17 (2), 414–422.

Flannagan, R.S., Jaumouillé, V., Grinstein, S., 2012. The cell biology of phagocytosis. Annual Rev. Pathol.: Mech. Disease 7, 61–98.

Flynn, K.C. et al., 2009. Growth cone-like waves transport actin and promote axonogenesis and neurite branching. Dev. Neurobiol. 69, 761–779.

Freeman, S.A., Grinstein, S., 2014. Phagocytosis: receptors, signal integration, and the cytoskeleton. Immunol. Rev. 262 (1), 193–215.

Fritzsche, M. et al., 2013. Analysis of turnover dynamics of the submembranous actin cortex. Mol. Biol. Cell 24 (6), 757–767.

Fujiwara, T. et al., 2002. Phospholipids undergo hop diffusion in compartmentalized cell membrane. J. Cell Biol. 157 (6), 1071–1082.

Gerhardt, M., Ecke, M., Walz, M., Stengl, A., Beta, C., Gerisch, G., 2014. Actin and PIP3 waves in giant cells reveal the inherent length scale of an excited state. J. Cell Sci. 127 (20), 4507–4517.

Gerisch, G., 2010. Self-organizing actin waves that simulate phagocytic cup structures. PMC Biophysics. 3, 7.

Gerisch, G., Schroth-Diez, B., Müller-Taubenberger, A., Ecke, M., 2012. PIP3 waves and PTEN dynamics in the emergence of cell polarity. Biophys. J. 103 (6), 1170–1178.

Griffin, F.M. et al., 1974. Segmental response of the macrophage plasma membrane to a phagocytic stimulus. J. Exp. Med. 139 (2), 323–336.

Griffin, F.M. et al., 1975. Studies on the mechanism of phagocytosis. I. Requirements for circumferential attachment of particle-bound ligands to specific receptors on the macrophage plasma membrane. J. Exp. Med. 142 (5), 1263–1282.

Guan, X., Guan, X., Dong, C., Jiao, Z., 2020. Rho GTPases and related signaling complexes in cell migration and invasion. Expt Cell Res. 388, (1) 111824.

Gu, H., Botelho, R.J., Yu, M., Grinstein, S., Neel, B.G., 2003. Critical role for scaffolding adapter Gab2 in FcγR-mediated phagocytosis. J Cell Biol. 161 (6), 1151–1161.

Hoppe, A.D., Swanson, J.A., 2004. Cdc42, Rac1, and Rac2 display distinct patterns of activation during phagocytosis. Mol. Biol. Cell 15 (8), 3509–3519.

Hu, J., Khamviwath, V., Othmer, Hans G., 2019. Othmer H.A stochastic model for actin waves in eukaryotic cells. bioRxiv.

Ikeda, Y. et al., 2017. Rac1 switching at the right time and location is essential for Fcγ receptor-mediated phagosome formation. J. Cell Sci. 130 (15), 2530–2540.

Inagaki, Naoyuki, Katsuno, Hiroko, 2017. Actin waves: Origin of cell polarization and migration?. Trends Cell Biol. 27 (7), 515–526.

Janmey, P.A. et al., 2018. Regulation of actin assembly by PI(4,5)P2 and other inositol phospholipids: an update on possible mechanisms. Biochem. Biophys. Res. Comm. 506 (2), 307–314.

Kamen, L.A., Levinsohn, J., Swanson, J.A., 2007. Differential association of phosphatidylinositol 3-kinase, SHIP-1, and PTEN with forming phagosomes. Mol. Biol. Cell 18 (7), 2463–2472.

Katsumi, Akira et al., 2004. Integrins in mechanotransduction. J. Biol. Chem. 297 (13), 12001–12004.

Khamviwath, Varunyu, Hu, Jifeng, Othmer, Hans G., et al., 2013. Othmer HG.A continuum model of actin waves in Dictyostelium discoideum. PloS One 8 (5). PMCID:PMC3669376.

Khatibi, S., Rios, K.I., Nguyen, L.K., 2018. Computational modeling of the dynamics of spatiotemporal rho GTPase signaling: A systematic review. In: Rho GTPases. Springer, pp. 3–20.

Killich, T., Plath, P.J., Haß, E.C., Xiang, W., Bultmann, H., Rensing, L., et al., 1994. Cell movement and shape are non-random and determined by intracellular, oscillatory rotating waves in Dictyostelium amoebae. Biosystems. 33 (2), 75–87.

Koda, Masato, Dogru, Ali H., Seinfeld, John H., 1979. Sensitivity analysis of partial differential equations with application to reaction and diffusion processes. J. Comput. Phys. 30 (2), 259–282.

Levin, R., Grinstein, S., Canton, J., 2016. The life cycle of phagosomes: formation, maturation, and resolution. Immunol. Rev. 273 (1), 156–179.

Liu, C., Deb, S., Ferreira, V.S., Xu, E., Baumgart, T., 2018. Kinetics of PTEN-mediated PI (3, 4, 5) P3 hydrolysis on solid supported membranes. PloS one 13, (2) e0192667.

Liu Y., Rens E.G., Edelstein-Keshet L. Spots, strips, and spiral waves in models for static and motile cells. arXiv preprint arXiv:190910504. 2019..

Masters, T.A., Sheetz, M.P., Gauthier, N.C., 2016. F-actin waves, actin cortex disassembly and focal exocytosis driven by actin-phosphoinositide positive feedback. Cytoskeleton. 73 (4), 180–196.

Miao, Y. et al., 2019. Wave patterns organize cellular protrusions and control cortical dynamics. Mol. Sys. Biol. 15, 3.

Mullins, R.D., Bieling, P., Fletcher, D.A., 2018. From solution to surface to filament: actin flux into branched networks. Biophys. Rev. 10 (6), 1537–1551.

Olivença, D.V., Uliyakina, I., Fonseca, L.L., Amaral, M.D., Voit, E.O., 2018. Pinto FR.A mathematical model of the phosphoinositide pathway. Sci. Rep. 8 (1), 1–12.

Pal, D.S., Li, X., Banerjee, T., Miao, Y., Devreotes, P.N., 2019. The excitable signal transduction networks: Movers and shapers of eukaryotic cell migration. Int. J. Dev. Biol.

Papayannopoulos, V. et al., 2005. A polybasic motif allows N-WASP to act as a sensor of PIP2 density. Mol. Cell. 17 (2), 181–191.

Rohatgi, R., HyH, Ho, Kirschner, M.W., 2000. Mechanism of N-WASP activation by CDC42 and phosphatidylinositol 4, 5-bisphosphate. J. Cell Biol. 150 (6), 1299–1310.

Roni, L. et al., 2015. Phosphoinositides in phagocytosis and macropinocytosis. Mol. Cell Biol. Lipids.

Rosales, C., Uribe-Querol, E., 2017. Phagocytosis: a fundamental process in immunity. BioMed Res Int. 2017.

Ryan, G.L., Petroccia, H.M., Watanabe, N., Vavylonis, D., 2012. Excitable actin dynamics in lamellipodial protrusion and retraction. Biophys. J. 102 (7), 1493–1502.

Saarikangas, J., Zhao, H., Lappalainen, P., 2010. Regulation of the actin cytoskeleton-plasma membrane interplay by phosphoinositides. Physiol. Rev. 90 (1), 259–289.

Salloum, G., Jaafar, L., El-Sibai, M., 2020. Rho A and Rac1: Antagonists moving forward. Tissue and Cell. 101364

Saltelli, Andrea et al., 2008. Global sensitivity analysis: the primer. John Wiley and Sons.

Schlam, D., Bagshaw, R.D., Freeman, S.A., Collins, R.F., Pawson, T., Fairn, G.D., et al., 2015. Phosphoinositide 3-kinase enables phagocytosis of large particles by terminating actin assembly through Rac/Cdc42 GTPase-activating proteins. Nature Comm. 6 (1), 1–12.

Schroth-Diez, B., Gerwig, S., Ecke, M., Hegerl, R., Diez, S., Gerisch, G., 2009. Propagating waves separate two states of actin organization in living cells. HFSP J. 3 (6), 412–427.

Scott, C.C., Dobson, W., Botelho, R.J., Coady-Osberg, N., Chavrier, P., Knecht, D.A., et al., 2005. Phosphatidylinositol-4, 5-bis phosphate hydrolysis directs actin remodeling during phagocytosis. J. Cell Biol. 169 (1), 139–149.

Sharma, V.P., Eddy, R., Entenberg, D., Kai, M., Gertler, F.B., Condeelis, J., 2013. Tks5 and SHIP2 regulate invadopodium maturation, but not initiation, in breast carcinoma cells. Current Biol. 23 (21), 2079–2089.

Singh, Shashi Prakash, Insall, Robert H., 2021. Adhesion stimulates Scar/WAVE phosphorylation in mammalian cells. Commun. Integrative Biol. 14 (1), 1–4.

Spill, Fabian et al., 2016. Effects of 3D geometries on cellular gradient sensing and polarization. Phys. Biol. 13, (3) 036008.

Swanson, J.A., Hoppe, A.D., 2004. The coordination of signaling during Fc receptor-mediated phagocytosis. J. leukocyte Biol. 76 (6), 1093–1103.

Tomasevic, N. et al., 2007. Differential Regulation of WASP and N-WASP by Cdc42, Rac1, Nck, and PI(4,5)P2. Biochemistry. 46, 3494–3502.

Vazquez, F., Matsuoka, S., Sellers, W.R., Yanagida, T., Ueda, M., Devreotes, P.N., 2006. Tumor suppressor PTEN acts through dynamic interaction with the plasma membrane. Proc. Nat. Acad. Sci. 103 (10), 3633–3638.

Vicker, M.G., 2002. Eukaryotic cell locomotion depends on the propagation of self-organized reaction-diffusion waves and oscillations of actin filament assembly. Exp. Cell Res. 275, 54–66.

Wasnik, V., Mukhopadhyay, R., 2014. Modeling the dynamics of dendritic actin waves in living cells. Phys. Rev. E 90, (5) 052707.

Weernik P.A.O. et.al. Activation of type I phosphatidylinositol 4-phosphate 5-kinase isoforms by the Rho GTPases, RhoA, Rac1, and Cdc42. J. Biol. 2004;279:7840–7849..

Weiner, O.D., Marganski, W.A., Wu, L.F., Altschuler, S.J., Kirschner, M.W., 2007. An actin-based wave generator organizes cell motility. PLoS Biol. 5 (9), 2053–2063.

Zhang, Y., Hoppe, A.D., Swanson, J.A., 2010. Coordination of Fc receptor signaling regulates cellular commitment to phagocytosis. Proc. Nat. Acad. Sci. 107 (45), 19332–19337.